

Title	Sensitivity of OWC performance to air compressibility
Authors	López, Iván;Carballo, Rodrigo;Taveira-Pinto, Francisco;Iglesias, Gregorio
Publication date	2019-06-20
Original Citation	López, I., Carballo, R., Taveira-Pinto, F. and Iglesias, G. (2019) 'Sensitivity of OWC performance to air compressibility', Renewable Energy, 145, pp. 1334-1347. doi: 10.1016/j.renene.2019.06.076
Type of publication	Article (peer-reviewed)
Link to publisher's version	http://www.sciencedirect.com/science/article/pii/S0960148119309048 - 10.1016/j.renene.2019.06.076
Rights	© 2019, Elsevier Ltd. All rights reserved. This manuscript version is made available under the CC BY-NC-ND 4.0 license. - https://creativecommons.org/licenses/by-nc-nd/4.0/
Download date	2025-08-03 13:34:08
Item downloaded from	https://hdl.handle.net/10468/8154

Sensitivity of OWC performance to air compressibility

I. López^{a,b}, R. Carballo^a, F. Taveira-Pinto^b, G. Iglesias^{c,d*}

^a University of Santiago de Compostela, Hydraulic Engineering, Campus Universitario s/n, 27002, Lugo, Spain.

^b Faculty of Engineering of the University of Porto, Department of Civil Engineering, Rua Dr. Roberto Frias, s/n, 4200-465, Porto, Portugal.

^c University College Cork, School of Engineering & MaREI, Environmental Research Institute, Cork, Ireland.

^d University of Plymouth, School of Engineering, Marine Building, Drakes Circus, Plymouth, PL4 8AA, United Kingdom.

Abstract

Air compressibility is often neglected in experimental work due to practical difficulties, even though it is known to affect the performance of OWC wave energy converters. The key question, of course, is to what extent. In this work the impact of air compressibility on the capture width ratio is thoroughly quantified by means of a comprehensive experimental campaign, with no fewer than 330 tests encompassing a wide range of wave conditions and levels of turbine-induced damping, and two experimental set-ups: one designed to account for air compressibility, the other to neglect it. This approach is complemented with the use of the RANS-based CFD model OpenFOAM[®] to calibrate the pressure-vs-flowrate curves, which enables the flowrate to be determined based on the pressure drop measurements from the physical model. We find that the errors that derive from disregarding air compressibility may lead to either under- or over-predictions of power output, and are highly dependent on the operating conditions, more specifically the wave conditions (sea state) and turbine-induced damping.

Keywords

wave energy; wave power; oscillating water column; physical modelling; CFD; capture-width ratio

1. Introduction

Over the last few decades, marine renewable energy has been identified as one of the renewable energy sources of greater potential, theoretically, enough to satisfy the global electric energy demand (Taveira-Pinto *et al.*, 2015). Among the different resources that integrate the marine renewables (waves, currents, tides, wind, thermal resources and salinity gradients), wave energy stands out by its

* Corresponding author
e-mail address: gregorio.iglesias@ucc.ie

high density and well-predictability (Arena *et al.*, 2015; Carballo *et al.*, 2015), its low environmental impact (Iglesias and Carballo, 2014), and an exploitability that fully synergizes with other marine renewable resources, such as offshore wind energy (Pérez-Collazo *et al.*, 2015), what enhances its economic viability (Astariz and Iglesias, 2015). Despite the efforts made to design efficient and reliable wave energy converters (WECs) (e.g., Contestabile *et al.*, 2017; López, M. *et al.*, 2017; Stansby *et al.*, 2015), there is no technology at a commercial stage yet. Hence, technological development is, doubtless, the key parameter for driving wave energy to the position that its potential deserves.

Among the different types of technologies developed to harvest wave energy, oscillating water column (OWC) devices (Falcão and Henriques, 2016) hold a prominent role. In fact, there are a number of OWC converters that have reached the stage of full-scale prototypes (e.g., Arena *et al.*, 2013; Ibarra-Berastegi *et al.*, 2018). An OWC consists mainly in an air turbine and a hollow chamber, partially submerged into the water and connected to the sea through an opening below the water surface. Wave action produces the oscillation of the water column inside the chamber—giving name to the device—and, subsequently, causes the alternating compression and decompression of the air above the water surface, generating an air flow rate which impulses the turbine coupled to a generator. Due to the bidirectional nature of the flow, a special air turbine design is needed. These self-rectifying turbines can be classified according to their operational principle as reaction or impulse type turbines. The reaction working principle has been applied to axial—the well-known Wells turbines (Raghunathan, 1995), radial (Moisel, Christoph and Carolus, 2014) and mixed-flow (Moisel, C. and Carolus, 2015) turbines. Similarly, both axial (Thakker *et al.*, 2004) and radial (Pereiras *et al.*, 2011) impulse type turbines have been developed. A comprehensive overview on self-rectifying turbines can be found in (Falcão and Gato, 2012).

The air pressure oscillations that takes place inside an OWC chamber and the subsequent air flow between the chamber and the atmosphere constitute complex thermodynamic processes that induce time-varying changes in air density. This spring-like effect of the air is known to significantly affect the performance of an OWC converter, as was demonstrated by means of analytical ideal-gas models, first, assuming an isentropic relationship between air pressure and density (Sarmiento and Falcão, 1985), and then, more realistically, considering changes in entropy due to viscous losses (Falcão and Justino, 1999). More recently, enhanced models based on the real-gas theory were also developed (Medina-López *et al.*, 2017). However, although constitute an essential step in WEC

development, analytical models do not consider important non-linear effects (e.g., wave breaking, viscosity or turbulence). Thus, physical or numerical models are a mandatory step in the design process of any converter. Computational fluid dynamic (CFD) techniques have shown to be capable to model OWC devices while accounting for all these effects (e.g., Elhanafi *et al.*, 2017; Simonetti *et al.*, 2018). Nevertheless, even the most advanced numerical models require a proper validation based on physical model tests.

In small-scale experimental tests, an appropriate modelling of the spring-like effects of air compressibility in the OWC chamber is not straightforward (Weber, 2007). In fact, to correctly reproduce these thermodynamic effects while assuming fully geometric similarity would require to control the ambient pressure to achieve a pressure ratio between model and prototype equal to the length scale ratio (Falcão and Henriques, 2014; Weber, 2007). As pointed by those authors, a feasible possibility to satisfy the scaling requirements of air compressibility is an appropriate adjustment of the air chamber volume, i.e., to not match full geometric similarity, at least in the aerodynamic domain of the OWC model. This is the methodology followed in the experimental model tests carried out by Sarmento (1993) and very recently by Perez-Collazo *et al.* (2018). However, despite the great amount of works published over the last few years dealing with physical modelling of OWC converters (e.g., Ning *et al.*, 2016; Vyzikas, Deshoulières, Barton *et al.*, 2017), references where the air compressibility effects are taken into account (if any) are scarcely found (Falcão and Henriques, 2016).

In this work, an extensive campaign of physical model tests was carried out in order to offer an in-depth evaluation of the effects of the air compressibility on the performance of an OWC wave energy converter, aiming to fully represent the complex physical relationships which other modelling methodologies may not be able to simulate, i.e., without requiring an analytical simplification of the governing processes. The testing campaign involved 330 tests, resulting from the combination of 55 regular wave conditions, three different levels of the turbine-induced damping and two set-up configurations. The associated difficulties related to the consideration of the spring-like effect of the air, required the use of numerical methods for calibrating the pressure-vs-flow-rate curves for the different values of the turbine-induced damping. For this purpose, the open-source CFD code OpenFOAM[®] was used as a complementary tool.

This paper is structured as follows. In Section 2, the materials and methods used to investigate the effects of the air compressibility on the performance of the OWC are detailed. First, the physical model campaign and its theoretical basis are presented. Second, the numerical model and its

characteristics (governing equations, computational domain, mesh and testing programme) are described. Last, the procedures to calculate the capture width ratio of the OWC are established. The results of the investigation are presented in Section 3, focusing on three main aspects: the validation of the numerical model; the pressure-vs-flow-rate curves of the orifices; and the analysis of the sensitivity of the OWC performance to air compressibility. Finally, conclusions are drawn in Section 4.

2. Materials and methods

2.1. Physical modelling

When designing a small-scale model of a wave energy converter—as in many other hydraulic applications in which free surface flows are involved—the Froude dynamic similitude criterion must be met (Hughes, 1993), i.e., equal Froude numbers in model and prototype. The Froude number (Fr) is defined as the ratio between the inertia (F_i) and gravity forces (F_g):

$$Fr = \frac{F_i}{F_g} = \frac{v^2}{gL} , \quad (1)$$

where v is a characteristic velocity; g is the gravitational acceleration; and L is a characteristic length of the system.

In OWC systems, however, the air compression forces also play an important role. In analogy to the formulation of the Froude number, a non-dimensional number to characterise the compression forces can be formulated (Weber, 2007) as the ratio of the inertia forces (F_i) to the air compression forces (F_c):

$$\frac{F_i}{F_c} = \frac{\rho v^2}{p_0 \gamma} , \quad (2)$$

where ρ is the fluid density; p_0 is the initial air pressure; and γ is the isentropic exponent. The simultaneous satisfaction of Eqs. (1) and (2) is far from straightforward and often impractical—it would require alterations of the fluid density or the control of the atmospheric pressure. The solution to overcome this (Falcão and Henriques, 2014) is to scale the air chamber volume according to:

$$\frac{V_m}{V_p} = \frac{n_m}{n_p} \varepsilon^2 \delta^{-1} , \quad (3)$$

where the subscripts m and p refer to model scale and prototype, respectively; V is the air volume of the OWC chamber at still water level; n is the polytropic exponent of the turbine; ε is the length scale ratio (L_m/L_p); and δ is the water density ratio (ρ_m/ρ_p).

In sum, an OWC model must ensure that the Froude similitude criterion is met in the hydrodynamic domain (taking into account the maximum elevation that could be achieved by the free surface oscillations) where, in addition, perfect geometric similarity between model and prototype is required (Sheng, Wan *et al.*, 2014); and a distorted air chamber (in the aerodynamic domain) with a volume that satisfies Eq.(3).

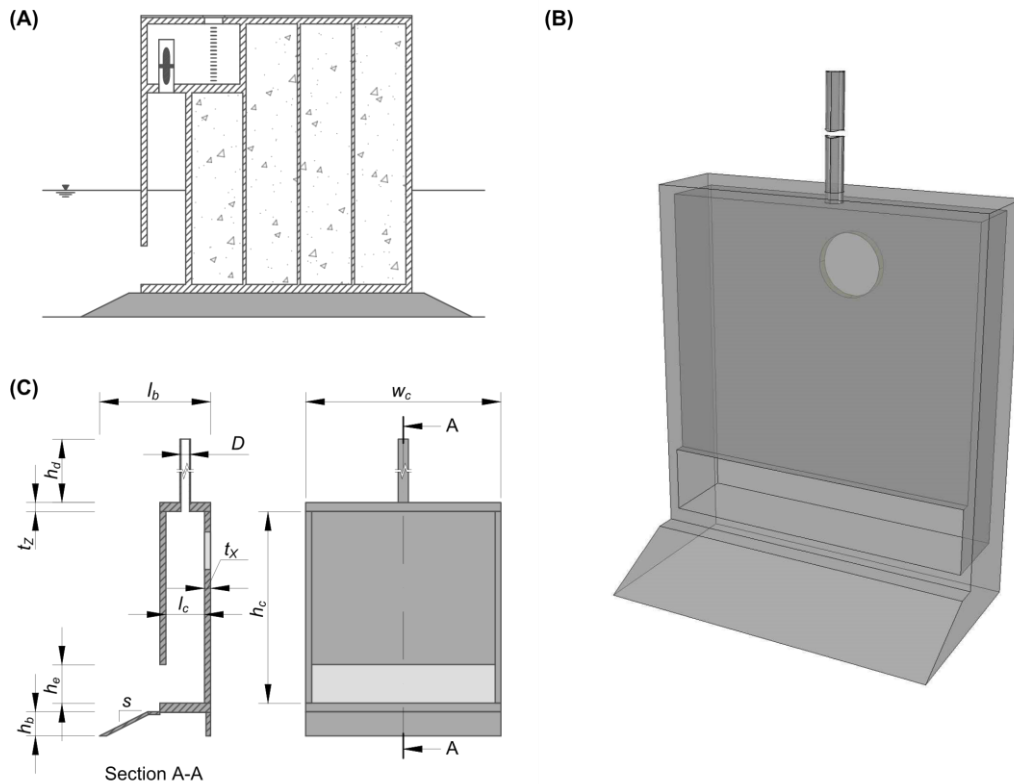


Figure 1. Schematic of (A) a breakwater-integrated OWC, and 3D perspective (B) and views (C) of the model OWC.

The tested OWC model was designed following this methodology. It corresponds to a 1:25 small-scale model of a regular design of breakwater-integrated OWC (Figure 1). A summary of the main dimensions of the model is presented in Table 1. It constitutes a 2D model in which the extra air chamber volume, needed to take into account the air compressibility effects, was achieved by connecting the chamber to an air reservoir of appropriate volume. This solution was successfully applied to other fixed-structure OWC devices (Sarmiento, 1993). In addition, using an air reservoir rather than a reshaped air chamber enables to assess the effects of the air compressibility on the performance of the OWC with one sole model, by connecting and disconnecting the air reservoir.

Table 1. Dimensions of the geometrical parameters of the OWC model

Geometrical parameter	Symbol	Model dimensions
Chamber height	h_c	63.6 cm
Chamber length (in the wave direction)	l_c	12.8 cm
Chamber width (transverse to wave direction)	w_c	65.0 cm
Entrance height	h_e	12.8 cm
Vertical walls thickness	t_z	2.0 cm
Horizontal walls thickness	t_x	2.8 cm
Orifice diameter	D	variable
Duct height	h_d	25D
Bedding height	h_b	8.0 cm
Bedding length	l_b	20.0 cm
Bedding slope	s	1:2

To simulate the turbine-induced damping—a critical variable in the performance of an OWC wave energy converter (López, I. *et al.*, 2014; Sheng, W. and Lewis, 2018)—an orifice was used, which emulates the quadratic pressure-versus-flow-rate relationship of a self-rectifying impulse turbine. In physical model tests, where the turbine can hardly be simulated by a small-scale turbine, using an orifice is a well-established method, in particular when dealing with scale factors below 1:10 (Falcão and Henriques, 2014), although it has also been applied in large-scale experiments (Viviano *et al.*, 2016). Three different values of the turbine-induced damping were used by varying the orifice diameter ($D = 28, 31$ and 39 mm). These three orifice diameters correspond, approximately, to an area of 0.8%, 1.0% and 1.5% of the plan area of the chamber, respectively; values which are in consonance with previous works (López, I. *et al.*, 2015).

The polytropic exponent of a turbine is related to the turbine efficiency (η) by (e.g., Dixon and Hall, 2014):

$$\eta = \frac{1 - (p_2/p_1)^{1-1/n}}{1 - (p_2/p_1)^{(\gamma-1)/\gamma}}, \quad (4)$$

where p_1 and p_2 are the pressures at the inlet and outlet of the turbine, respectively; and the isentropic exponent takes the value of $\gamma = 1.4$ for air. Therefore, the polytropic exponent is a function of the turbine efficiency and the pressure ratio (p_2/p_1). Falcão and Henriques (2014) have shown that the polytropic exponent is approximately constant with respect to the pressure ratio and varies depending on the turbine efficiency between $n = 1$ for the case in which no work is done by the turbine ($\eta = 0$) and $n = 1.4$ for a perfectly efficient turbine ($\eta = 1$). Thus, in the case of a turbine simulated by an orifice the polytropic exponent is $n = 1$. For a state-of-the-art full-size turbine, with an average efficiency of about $\eta = 0.6$, the polytropic exponent is approximately $n = 1.2$ (Falcão and Henriques, 2016). Taking into account these values ($n_m = 1$ and $n_p = 1.2$) together with the dimensions of the

OWC to be tested (Table 1), and considering a water density ratio for wave flume testing of $\delta = 0.98$, the air volume of the chamber at 1:25 scale should be, applying Eq.(3), $V_m = 538.4 \text{ dm}^3$. After subtracting the air volume already contained inside the model chamber (25.2 dm^3) and the air volume contained inside the duct that connects the chamber and the reservoir (18.2 dm^3), the air volume that the reservoir has to supply is equal to 495 dm^3 . In the present application, an iron reservoir was used (Figure 2), partially filled with water to remove the volume in excess of the desired one. Care must be taken when designing and constructing the reservoir, as it must resist the pressures generated by the OWC model without becoming deformed, which if happened would introduce undesired effects into the system; similarly, the duct diameter should not be too small.

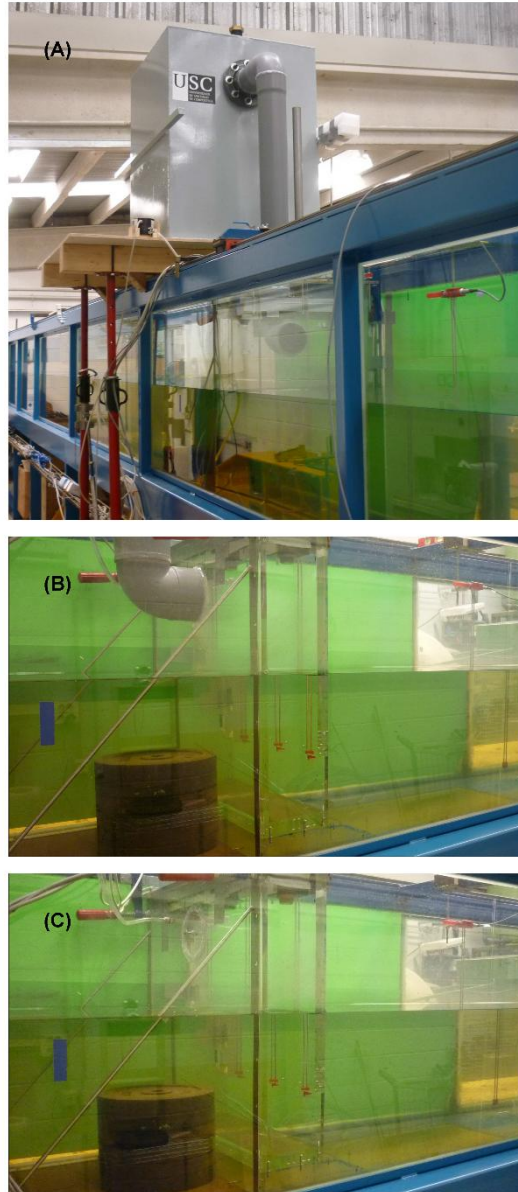


Figure 2. Photographs of (A) a general view of the air reservoir and its connection duct; (B) a detailed view of the connection of the duct to the OWC chamber; and (C) detail of the incompressible set-up without air reservoir.

2.1.1. Experimental testing programme and set-up

In order to thoroughly characterise the performance of the OWC, a total of 55 regular wave conditions were tested, resulting from the combination of five wave heights (H), from $H = 0.02$ m to $H = 0.10$ m, in increments of 0.02 m (from $H = 0.5$ m to $H = 2.5$ m, in prototype dimensions) and eleven wave periods (T), from $T = 1.0$ s to $T = 3.0$ s, in increments of 0.2 s (from $T = 5.0$ s to $T = 15.0$ s, in prototype dimensions). The water depth (h) was set to 0.42 m ($h = 10.5$ m, in prototype dimensions). The 55 wave conditions were tested for the three aforementioned orifice diameters ($D = 28, 31$ and 39

mm), representative of three different values of the turbine-induced damping. In addition, tests were carried out under two different set-ups: (i) taking into account the air compressibility effects by scaling the chamber air volume proportionally to the square of the scale factor, Eq.(3), (i.e., connecting the air chamber to the air reservoir); and (ii) assuming air incompressibility at model scale by scaling the chamber air volume with the cube of the scale factor (i.e., disconnecting the air reservoir). In total, the experimental campaign comprised 330 tests.

Tests were carried out in the wave flume of the University of Santiago de Compostela, Spain. The flume is 20 m long, 0.95 m high and 0.65 m wide. A piston-type paddle, equipped with an active wave absorption system, *DHI AWACS* (Schäffer and Jakobsen, 2003), that prevents re-reflections of incoming waves, was used for wave generation. The experimental set-up is presented in Figure 3. The OWC model was located at 10.30 m from the paddle, with the air reservoir placed at the rear top of the chamber. Free surface elevation was measured using nine *DHI-202* resistance wave gauges (WGs) distributed along the flume (Figure 3). The measurements of the gauges enabled the monitoring of the incident waves (WG1), the analysis of the incident and reflected waves fields (WG2-5), the verification the waves approaching the model (WG6), and the verification of the absence of transverse waves (WG7-9). Additionally, two *Omega-LVU31* ultrasonic level sensors (US1 and US2) were placed inside the chamber to record the oscillations of the water column. Both types of level sensors, resistance wave gauges and ultrasonic level sensors, have resolutions below 1 mm with an accuracy of millimetres. Finally, the pressure drop between the interior of the chamber and the atmosphere was measured by means of a *GE-Druck-LPM5480* differential pressure sensor (PS), with a range of ± 2000 Pa and accuracy of $\pm 0.25\%$ of full scale. The sampling frequency of all the measurement instrumentation was 20 Hz.

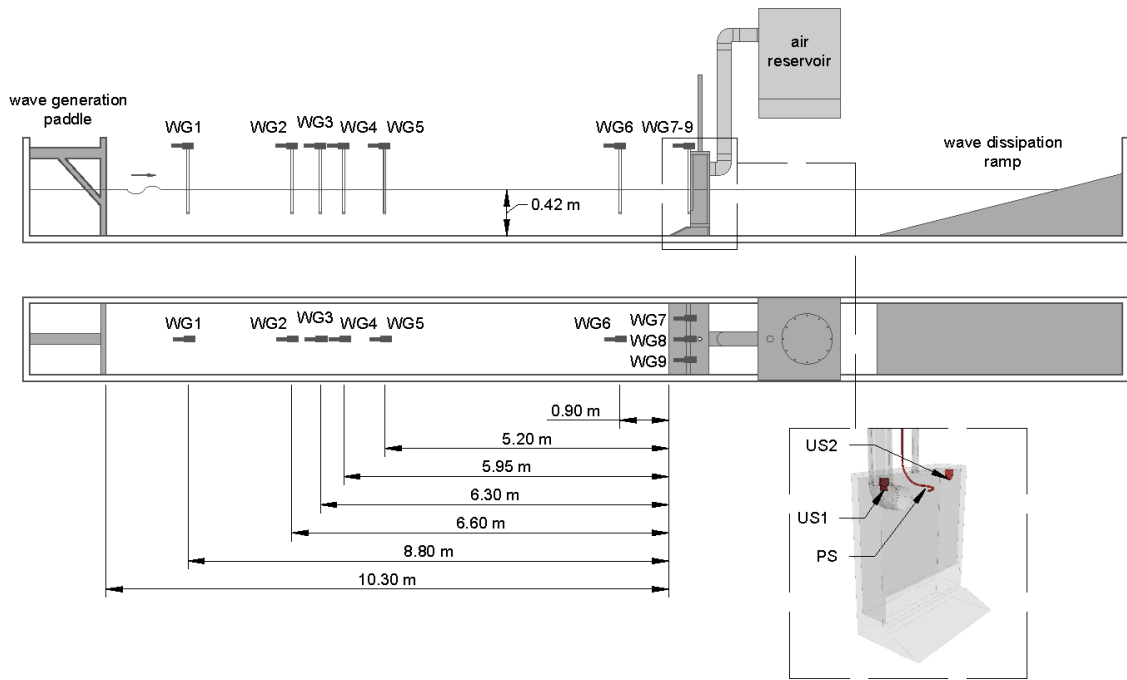


Figure 3. Experimental set-up.

The main caveat when considering air compressibility is the measurement of the air flow rate that, after taking into account the air compressibility, cannot be directly calculated from the motions of the free surface within the chamber. The first attempt was to use an air flow rate meter—hence the use of the duct. Nevertheless, the operational conditions are very demanding (bidirectional flow of relatively high frequency, variable range and high accuracy requirements) and the checked solutions did not show a successful performance. The most common alternative is the calibration of the orifice in order to obtain the relation between the pressure drop and the circulating air flow rate (Sarmento, 1993; Sheng, W. *et al.*, 2013). In this case, the calibration was accomplished through numerical modelling.

Given the small values of the pressure drop ratio (defined as the ratio between the pressure drop through the orifice and the absolute pressure on the inlet side) achieved in the model tests, the expansibility factor of air (Y), which corrects for expansion effects when a compressible fluid passes through an orifice, would become very close to unity, $Y > 0.99$ (Reader-Harris, 2015), which means that the calibration of the orifice remains constant regardless of the air compressibility. This fact enables an incompressible numerical model to be used to calibrate the orifice. Once calibrated, the obtained curves allowed the air flow rate to be computed in the physical model directly from the pressure drop measurements.

2.2. Numerical modelling

The open-source computational fluid dynamics (CFD) package OpenFOAM[®] (version 4.1) was used for modelling the OWC. It is a bundle of different C++ libraries capable of solving a wide variety of continuum mechanics problems (Jasak *et al.*, 2007). Among the different solvers included in the OpenFOAM[®] package, for solving the motions of the interface between two incompressible phases the *interFoam* solver was used. OpenFOAM[®] has been successfully used and validated to deal with OWC modelling, both to analyse the hydrodynamics of the device (Vyzikas, Deshoulières, Giroux *et al.*, 2017) and to optimise the geometry and the turbine-induced damping (Simonetti *et al.*, 2017).

2.2.1. Governing equations

The numerical model solves the Reynolds averaged Navier–Stokes (RANS) equations, which describe the flow motion of a fluid. The RANS equations consist of a mass conservation equation, Eq.(5), and a momentum conservation equation, Eq.(6), expressed as:

$$\frac{\partial u_i}{\partial x_i} = 0 \quad , \quad (5)$$

$$\frac{\partial \rho u_i}{\partial t} + u_j \frac{\partial \rho u_i}{\partial x_j} = -\frac{\partial p^*}{\partial x_i} - g_i X_j \frac{\partial \rho}{\partial x_j} + \frac{\partial}{\partial x_j} \left[\mu_{eff} \frac{\partial u_i}{\partial x_j} \right] + f_{\sigma,i} \quad , \quad (6)$$

where $i, j = 1, 2, 3$ denote the Cartesian components of the three-dimensional vectors or tensors; u_i is the i th component of the velocity vector; ρ is the density of the fluid; p^* is the pseudo-dynamic pressure; g_i is i th component of the gravitational acceleration; X_i is the position vector; μ_{eff} is the effective dynamic viscosity ($\mu_{eff} = \mu + \rho \nu_t$, where μ is the molecular dynamic viscosity and ν_t is the turbulent kinematic viscosity given by the turbulence model); finally, $f_{\sigma,i}$ is the i th component of the surface tension tensor term.

As mentioned above, a turbulence model which provide a value for the turbulent kinematic viscosity is needed for the closure of the equations. In this case, the $k-\omega$ SST turbulence model was used. This model combines the best features of the $k-\epsilon$ and $k-\omega$ models showing good results in simulating OWC devices (Iturrioz *et al.*, 2015), other wave energy conversion technologies (Schmitt and Elsaesser, 2015) and also wave-structure interaction problems in coastal engineering (Higuera *et al.*, 2013).

The movements of the interface between the air and water phases was tracked by the volume-of-fluid (VOF) method (Hirt and Nichols, 1981). This method uses a phase-fraction function (α) defined as the fraction of the cell volume filled with water: for a cell full of water the phase-fraction function

takes a value of $\alpha = 1$, for a cell full of air $\alpha = 0$, and $0 < \alpha < 1$ for an interface cell which contains both air and water. The tracking of the free surface movements is modelled by means of the following advection equation:

$$\frac{\partial \alpha}{\partial t} + \frac{\partial u_i \alpha}{\partial x_i} + \frac{\partial u_{c,i} \alpha (1 - \alpha)}{\partial x_i} = 0, \quad (7)$$

where the last term on the left-hand-side is an artificial compression term (Deshpande *et al.*, 2012) introduced to achieve a sharper interface, being $u_{c,i}$ the artificial compression velocity.

For wave generation and absorption, the relaxation technique included in the *waves2Foam* toolbox was used (Jacobsen *et al.*, 2012). This technique forms part of the internal wave generation methods, in which waves are generated within a region defined inside the numerical domain. In addition, the relaxation zones enable passive wave absorption to avoid reflection of waves into the computational domain. Thus, wave generation and absorption are accomplished by modifying the velocity, pressure and phase-fraction function inside the relaxation zone following:

$$\phi = \alpha_R \phi_{computed} + (1 - \alpha_R) \phi_{target}, \quad (8)$$

where ϕ represents any flow variable in the relaxation zone for which the solution will be a weighted combination of the numerical model solution and a target or desired solution forced over the relaxation zone; and α_R is the relaxation function, defined as (Jacobsen *et al.*, 2012):

$$\alpha_R(\chi_R) = 1 - \frac{\exp(\chi_R^{3.5}) - 1}{\exp(1) - 1} \quad \text{for } \chi_R \in [0, 1], \quad (9)$$

where χ_R is the coordinate along the x -axis scaled to the length of the relaxation zone.

2.2.2. Computational domain

The numerical model faithfully reproduces the experimental set-up, with the differences inherent to numerical wave generation through relaxation zones, that is, the numerical wave flume incorporates an upstream extra section—the relaxation zone region (Figure 4)—where waves are generated and absorbed, emulating the wave generation and absorption system of the experimental wave flume.

There is no outlet relaxation zone as no waves go beyond the OWC model; for the same reason, the numerical flume ends just behind the OWC. Furthermore, the numerical model takes advantage of a symmetry boundary condition to only simulate one half of the flume, which brings important computational cost savings. The length of the computational domain from the end of the relaxation zone (where wave propagation starts) to the front wall of the OWC model was set, as in the experimental set-up, to 10.30 m.

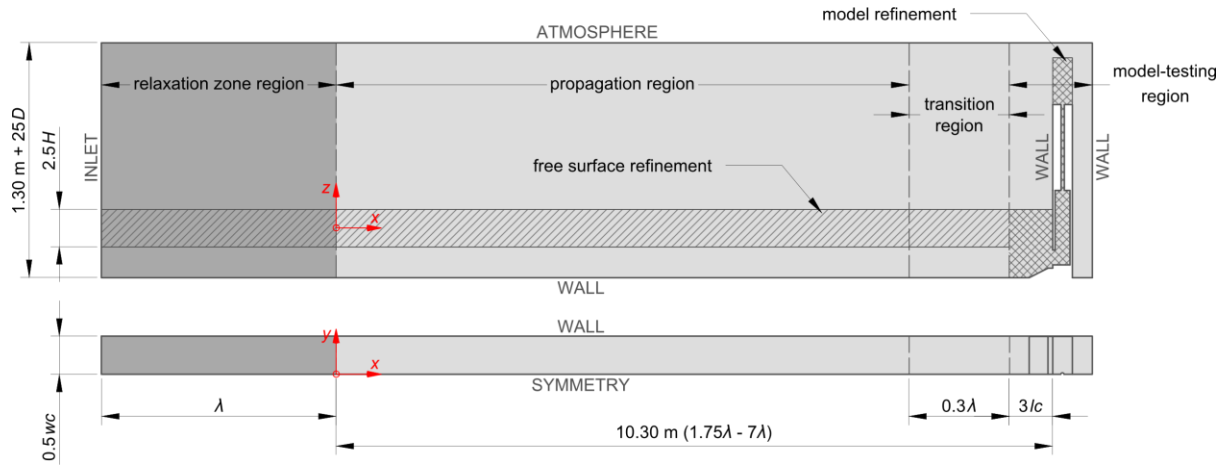


Figure 4. Computational domain. The boundary conditions are indicated in capital letters.

The computational domain was spatially discretised using the *snappyHexMesh* utility, a mesh generator which, starting from a simple background mesh that is iteratively refined and morphed, outputs a hexahedral mesh conformed to a given geometric surface. Attending to the characteristics of the mesh, four main regions can be distinguished (Figure 4): the relaxation region, the propagation region, the transition region and the model-testing region. In the three first regions (relaxation, propagation and transition regions) the mesh is parameterised based on the wave conditions to be simulated, i.e., the cell size varies depending on the wave height and the wave period. The characteristics of the model-testing zone, however, remains constant despite changes in the wave conditions. With this methodology of different mesh regions, a uniform grid with a cell aspect ratio equal to one—optimum for the performance of the *snappyHexMesh* utility—can be generated in the location of the OWC model, without affecting the mesh of the remaining domain. The computational mesh is presented in Figure 5.

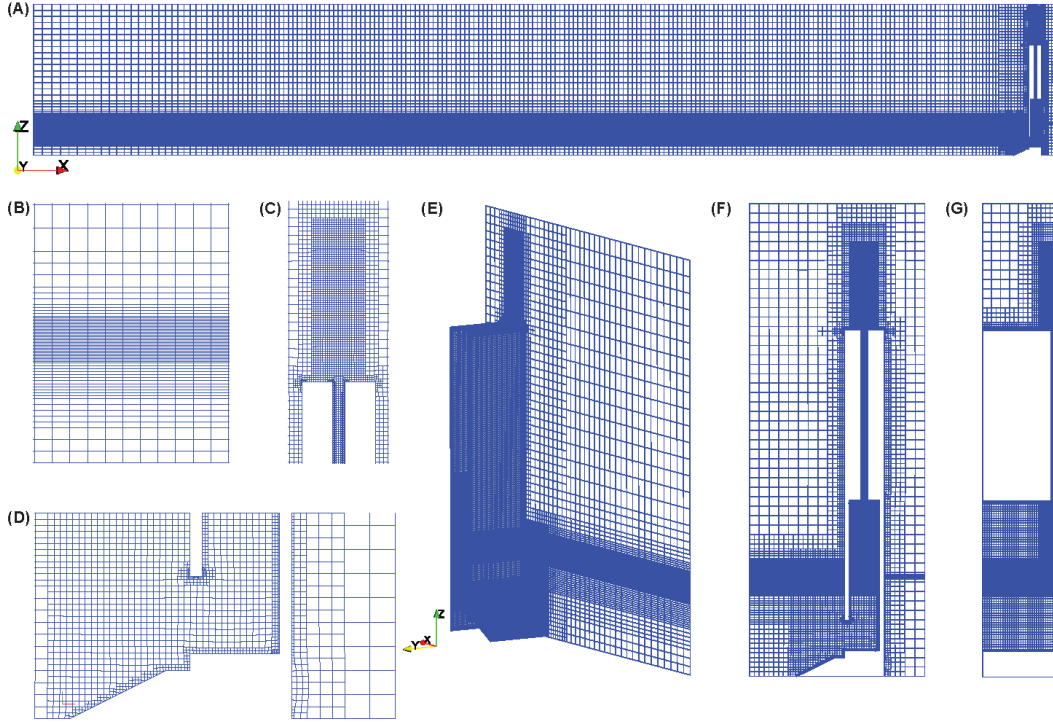


Figure 5. Computational mesh: (A) general view of the numerical wave flume; (B) detail of the mesh around the free surface; (C) detail of the mesh around the outlet of the orifice; (D) detail of the mesh around the entrance of the chamber; (E) perspective view zoomed in the model-testing region; (F) slice orthogonal to the y -axis at $y = 0$ (symmetry boundary); and (G) slice orthogonal to the x -axis at $x = 10.384$ m (x -coordinate of the centre of the orifice).

In the propagation region, the mesh is uniform along the x -axis, with a cell size that ensures 50 cells per wavelength, a value already used in similar applications (Vanneste and Troch, 2015). As mentioned above, the length of this region is constant in order to faithfully reproduce the experimental set-up; therefore, following previous works (López, I. *et al.*, 2014), a non-uniform mesh was set along the z -axis, with a finer sub-mesh around the free surface. The minimum cell size was set to $\Delta z = 0.005$ m for $H = 0.04$ - 0.06 m, and to $\Delta z = 0.010$ m for $H = 0.08$ - 0.10 m, to match the ratio $H/\Delta z \geq 8$ (Simonetti *et al.*, 2017). For the smallest waves ($H = 0.02$ m) it was found that a ratio $H/\Delta z \geq 2$ is enough (Vanneste and Troch, 2015), so the cell size was set to $\Delta z = 0.005$ m. As the distance to the free surface increases, the cell size is doubled successively, maintaining the cell size constant during, at least, three layers. The growth is faster towards the air domain where a maximum cell size of $\Delta z = 0.08$ m was set. Those settings, both on the x - and z -axis, were maintained in the relaxation region, whose total length was established to one wavelength, a solution successfully employed in upstream relaxation zones (e.g., Hu *et al.*, 2016; Simonetti *et al.*, 2017). The z -axis settings of the propagation region were maintained, again, in the transition region. However, along the x -axis a growing rate was established to ensure a smooth transition from the cell size in the

propagation region to that in the model-testing region. The total length of the transition region was set to 0.3 wavelength. In these three regions, the cell size in the y-axis was set to $\Delta y = 0.04$ m, resulting in 8 cells along this axis; which is enough as no meaningful flow is expected in this direction.

Finally, in the un-parametrized mesh of the model-testing region a base cell size of $\Delta x = \Delta y = \Delta z = 0.04$ m was used. This base size was refined progressively in all directions (using up to five refinement levels) in the proximity of the OWC model contours to obtain a mesh that better fits the model. A minimum of two cell layers of each size was established to improve the mesh smoothness. The area in the interior of the chamber and at the front of the OWC model was refined to $\Delta x = \Delta y = \Delta z = 0.01$ m and at the free surface to $\Delta x = \Delta y = \Delta z = 0.005$ m. In addition, an extra refinement was made in the orifice duct and its inlet and outlet area matching that of the free surface.

The boundary conditions were set to *wall* for the bottom, left-side, and rear boundaries, as well as for all the boundaries of the OWC model (Figure 4). The *wall* boundary condition implies no-slip condition for velocity, zero-gradient conditions for pressure and phase-fraction function, and special wall functions for k and ω according to the k - ω SST turbulence model. At the *inlet*, special wave generating functions were implemented for velocity and phase-fraction (Jacobsen *et al.*, 2012), whereas zero-gradient conditions were set for pressure. At the *atmosphere*, the pressure was set to a fixed total value equal to zero, the velocity to a *pressureInletOutletVelocity* condition in which a zero-gradient condition is applied for outflow, and for inflow the velocity is calculated from the flux through the boundary; the phase-fraction function was set to an *inletOutlet* condition, which switches between zero-gradient for outflow, and a fixed value set to zero (air), for the case of return flow. Finally, the right-side of the computational domain was set to a symmetry boundary.

2.2.3. Numerical testing programme

The aim of the numerical tests is the calibration of the three orifices that emulate the turbines. Given that the pressure-vs-flow-rate depends on the characteristics of the orifice, and not on the wave conditions that forced them (Sheng, W., Thiebaud *et al.*, 2013), calibrating the orifices for the whole set of wave conditions is not necessary. In any case, a heterogeneous selection of nine wave conditions were tested to prove the previous statement, covering five different wave periods and five wave heights (Table 2).

340

Table 2. Wave conditions included in the numerical testing programme.

Wave condition	Model dimensions		Prototype dimensions	
	<i>T</i>	<i>H</i>	<i>T</i>	<i>H</i>
#1	1.20 s	0.06 m	6 s	1.5 m
#2	1.60 s	0.02 m	8 s	0.5 m
#3	1.60 s	0.04 m	8 s	1.0 m
#4	1.60 s	0.06 m	8 s	1.5 m
#5	1.60 s	0.08 m	8 s	2.0 m
#6	1.60 s	0.10 m	8 s	2.5 m
#7	2.00 s	0.06 m	10 s	1.5 m
#8	2.40 s	0.06 m	12 s	1.5 m
#9	2.80 s	0.06 m	14 s	1.5 m

341 However, the first milestone when dealing with numerical modelling is the validation. In this
 342 case, it was carried out through the comparison between the experimental measurements (from the
 343 incompressible set-up) and the numerical model data. The heterogeneity of the wave conditions
 344 selected for the numerical programme ensure a meaningful validation without reproducing the whole
 345 experimental set. In order to validate the model, both the pressure drop between the interior of the
 346 chamber and the atmosphere, and the oscillations of the water column were measured. Additionally,
 347 the free surface elevations along the flume were measured at the same positions defined in the
 348 experimental set-up (Figure 3). The flow rate through the orifice was also measured for calibrating the
 349 orifice.

350 The performance of the numerical model for each wave condition was evaluated on the basis of
 351 the correlation coefficient and the normalised root mean square error (Appendix A).

352 2.3. Data analysis

353 Once the numerical model was validated, the next step was to obtain the calibration curves of the
 354 three orifices. For each numerical test, the data points of pressure drop versus flow rate were fitted
 355 with a parabolic curve centred at the origin (López, I. *et al.*, 2016) that can be expressed, for
 356 exhalation stage ($\Delta p > 0$) by:

$$357 \quad \Delta p = B_{exh} Q^2, \quad (10)$$

358 and for inhalation stage ($\Delta p < 0$) by:

$$359 \quad \Delta p = -(B_{inh}) Q^2, \quad (11)$$

360 where Δp is the pressure drop between the interior of the chamber and the atmosphere, Q is the flow
 361 rate and B is a damping parameter. The damping parameters for each orifice were calculated as the
 362 average of the nine damping parameter values obtained from the wave conditions tested. Given the
 363 closeness between the inhalation and exhalation values, a representative damping parameter (B_r) was

subsequently calculated as the average of the values of both stages. Finally, based on previous works (López, I. *et al.*, 2014), a dimensionless damping coefficient was defined as:

$$B^* = \frac{\Delta p^{1/2}}{Q} \frac{A_c}{\rho_a^{1/2}} = B_r^{1/2} \frac{A_c}{\rho_a^{1/2}} , \quad (12)$$

where A_c is the plant area of the OWC chamber ($A_c = l_c \times w_c$); and ρ_a is the air density. The damping coefficient is, therefore, a dimensionless parameter that characterises the turbine-induced damping.

From the numerical obtained damping parameters of the three orifices and the experimental pressure drop data, the instantaneous flow rate for each one of the 330 experimental tests was calculated following:

$$Q = \text{sgn}(\Delta p) \left(\frac{|\Delta p|}{B_r} \right)^{1/2} . \quad (13)$$

Known the instantaneous pressure drop and the flow rate, the mean pneumatic power is given by:

$$P_p = \frac{1}{t_{max}} \int_0^{t_{max}} \Delta p Q dt . \quad (14)$$

Once the pneumatic power is calculated, the second key variable to evaluate the performance of an OWC is the wave power. First, the incident and reflected wave fields were obtained by means of a reflection analysis carried out using the Mansard and Funke (Mansard and Funke, 1980) method modified by Baquerizo (1995). Second, based on the incident wave spectrum the mean power of the incident waves per unit width of converter was computed as:

$$P_w = \rho_w g \int_0^\infty S(\omega) c_g(\omega) d\omega , \quad (15)$$

where ρ_w is the water density; $S(\omega)$ is the spectral density; and c_g is the group velocity, defined as:

$$c_g = \frac{1}{2} \left(1 + \frac{2kh}{\sinh(2kh)} \right) \frac{\omega}{k} , \quad (16)$$

where k is the wave number; h is the water depth; and ω is the angular frequency, which is obtained from the dispersion relationship:

$$\omega^2 = gk \tanh(kh) . \quad (17)$$

Finally, the capture width ratio (also known as relative capture width) of the OWC, i.e., the efficiency in transforming the power of the incoming waves into pneumatic power, is defined as:

$$C_{WR} = \frac{P_p}{w_c P_w} . \quad (18)$$

where w_c is the width of the OWC chamber (Figure 1).

3. Results and discussion

3.1. Numerical model validation

The results of the numerical model validation for the pressure drop and the free surface elevation inside the OWC chamber are summarised in Table 3. Excellent agreement is found, with an average value of the correlation coefficient for the entire validation set close to unity and a NRMSE well below 10%, both for pressure drop ($R = 0.992$, NRMSE = 7.29%) and free surface elevation ($R = 0.986$, NRMSE = 5.90%). Although a slight performance decrease is observed when the orifice diameter increases, the results are good and consistent for the three orifice diameters tested. Comparing the results between the pressure drop and free surface elevation signals, a better agreement is found for the latter, as shows the lower value of the NRMSE: 7.29% for pressure drop vs 5.90% for the free surface elevation. The magnitude of the errors is of the same order of those achieved in previous OWC numerical models, either using an OpenFOAM® code (e.g., Simonetti *et al.*, 2017) or different commercial codes (e.g., López, I. *et al.*, 2014).

Table 3. Results of the numerical model validation based on the comparison between the experimental and numerical signals of pressure drop (Δp) and free surface elevation inside the OWC chamber (η_{owc}).

D (mm)	Δp				η_{owc}			
	R		NRMSE		R		NRMSE	
	average	s	average	s	average	s	average	s
28	0.9922	0.0044	0.0680	0.0186	0.9878	0.0044	0.0547	0.0131
31	0.9956	0.0073	0.0645	0.0204	0.9867	0.0050	0.0592	0.0117
39	0.9878	0.0097	0.0861	0.0316	0.9844	0.0113	0.0632	0.0159
	0.9919	0.0079	0.0729	0.0252	0.9863	0.0074	0.0590	0.0136

The excellent agreement is qualitatively illustrated in Figure 6, which shows the superposition of the pressure drop and free surface elevation inside the chamber from both models, physical and numerical. For clarity, only 10 s of simulation are presented. The agreement found is, again, very good. Thus, both the amplitude and the period of the pressure drop and the water column oscillations are well reproduced by the numerical model for the three orifice diameters tested. As was previously found by means of the NRMSE, the performance of the model is shown to better reproduce the free surface elevations of the water column than the pressure drop, with the amplitude of the latter slightly overpredicted. It should also be noted, that the phase between both signals is well reproduced by the numerical model too, which is paramount for a correct reproduction of the pressure-vs-flow-rate curves.

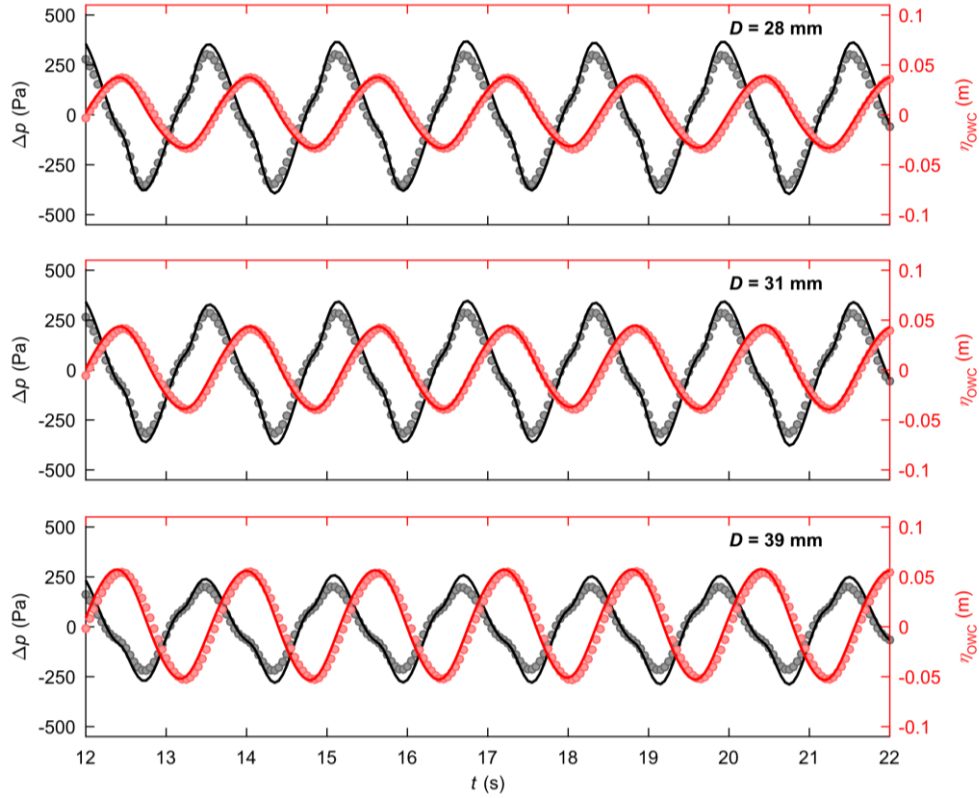


Figure 6. Pressure drop (black) and free surface elevations of the water column inside the chamber (red) corresponding to a wave condition with $H = 0.06$ m and $T = 1.6$ s, for the three orifice diameters tested (— numerical model; \circ physical model).

Furthermore, the time series of free surface elevations obtained from the physical and numerical models at two positions, one at the middle of the flume and the other in front of the OWC model, i.e., at WG4 and WG6 (Figure 3), are also compared, first, in Figure 7, for the wave condition with the smallest wave height ($H = 0.02$ m; $T = 1.6$ s), and second, in Figure 8, for the wave condition with the largest wave height ($H = 0.10$ m; $T = 1.6$ s). The agreement found for both wave conditions is, as in the previous validation cases, excellent. Both the wave height and period are well reproduced by the numerical model all along the flume, as show the matching between the signals measured and computed at WG4 and WG6 positions. In general, the agreement is slightly higher for the smaller waves, which is probably due to their being better represented through linear theory. Interestingly, it can be seen that the amplitude of the wave profiles varies depending on the diameter of the orifice considered. This is due to the different energy absorption of the OWC for each orifice and, consequently, to the variation in existing reflected waves.

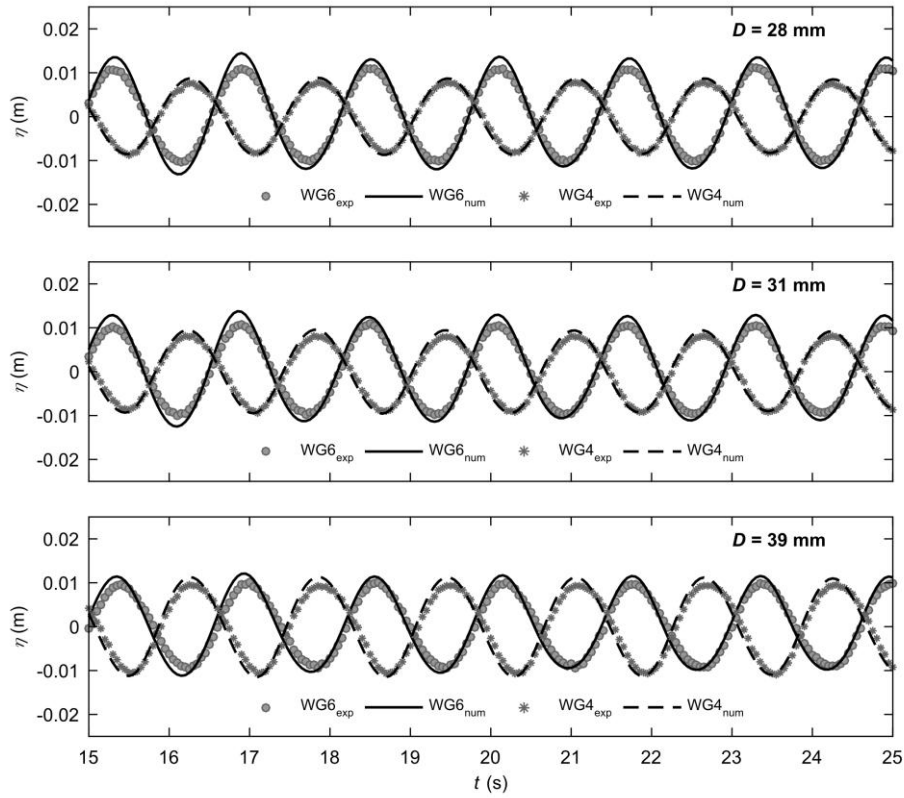


Figure 7. Time series of free surface elevation (η) at WG4 and WG6 positions, corresponding to a wave condition with $H = 0.02$ m and $T = 1.6$ s, for the three orifice diameters tested.

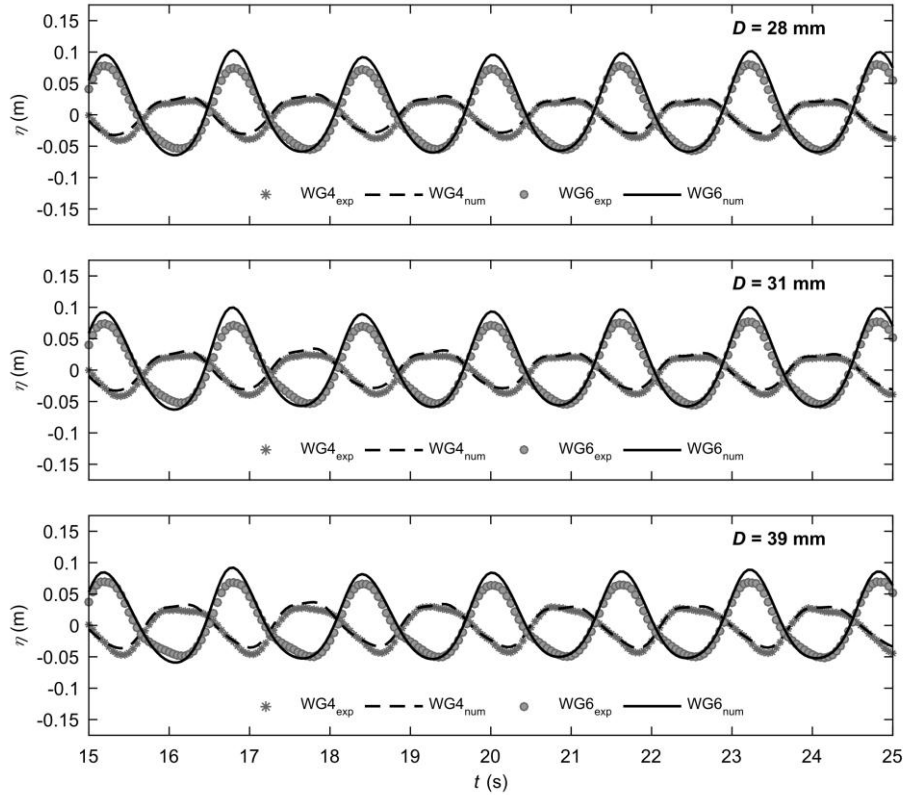


Figure 8. Time series of free surface elevation (η) at WG4 and WG6 positions, corresponding to a wave condition with $H = 0.10$ m and $T = 1.6$ s, for the three orifice diameters tested.

The quantitative results of the validation of the free surface elevation at WG4 and WG6 positions are presented in Table 4. The average value of the correlation coefficient is, for the two wave conditions and at both positions, close to unity ($R > 0.98$). Similarly, the NRMSE is well below 10%, both for the smallest and the largest wave, although it is slightly higher in the case of the latter.

Table 4. Results of the numerical model validation based on the comparison between the experimental and numerical signals of free surface elevation at two positions along the flume (η_{WG4} and η_{WG6}), for two different wave conditions.

<i>D</i> (mm)	<i>H</i> = 0.02 m, <i>T</i> = 1.6 s				<i>H</i> = 0.10 m, <i>T</i> = 1.6 s			
	η_{WG4}		η_{WG6}		η_{WG4}		η_{WG6}	
	<i>R</i>	NRMSE	<i>R</i>	NRMSE	<i>R</i>	NRMSE	<i>R</i>	NRMSE
28	0.9983	0.0635	0.9960	0.0379	0.9952	0.0816	0.9886	0.0806
31	0.9974	0.0665	0.9948	0.0443	0.9967	0.0859	0.9863	0.0835
39	0.9857	0.0718	0.9839	0.0708	0.9950	0.0823	0.9884	0.0776
	0.9938	0.0673	0.9916	0.0510	0.9956	0.0833	0.9878	0.0806

All in all, the results of the validation process demonstrate that the numerical model implemented accurately reproduces the behaviour of an OWC wave energy converter under different values of the turbine-induced damping.

3.2. Orifice calibration curves

Once validated, the numerical model was used to extract the pressure-vs-flow-rate curves for the three orifice diameters, corresponding to three different values of the turbine-induced damping. The data points and the parabolic curves which fit them for each one of the orifice diameters are presented in Figure 9. The values of the representative damping parameter for each damping condition are presented in Table 5.

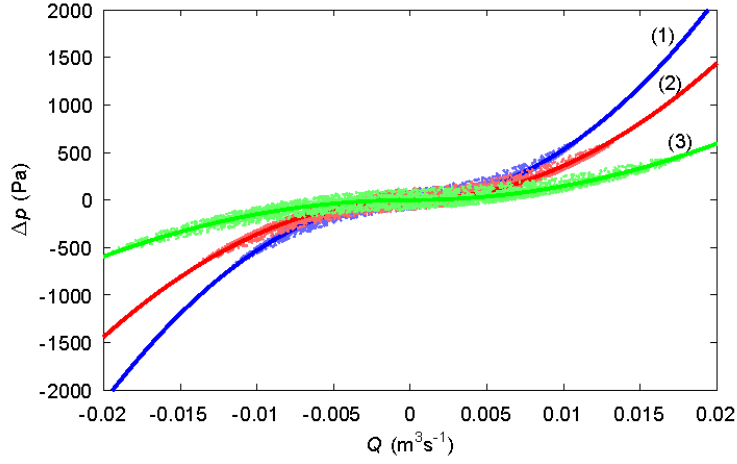


Figure 9. Data points of pressure drop vs flow rate and the corresponding parabolic curves (inhalation and exhalation) for the three orifice diameters tested: (1) $D = 28$ mm; (2) $D = 31$ mm; and (3) $D = 39$ mm.

The agreement between the dataset and the fitted curves is very good, which confirms the quadratic pressure-vs-flow-rate relationship. Furthermore, it indicates that the damping parameters are consistent regardless of the wave height and wave period. This statement is also corroborated by the low values of the standard deviation presented in Table 5. Given the small difference between the inhalation and exhalation values of the damping parameter, the use of an average representative value for both stages (B_r) is justified.

Table 5. Inhalation, exhalation and representative values of the damping parameter (B) for the three orifice diameters tested.

D (mm)	B_{inh} (kg/m ⁷)		B_{exh} (kg/m ⁷)		B_r (kg/m ⁷)
	average	s	average	s	average
28	5.33×10^6	9.72×10^4	5.27×10^6	8.24×10^4	5.30×10^6
31	3.59×10^6	7.54×10^4	3.59×10^6	6.86×10^4	3.59×10^6
39	1.48×10^6	3.59×10^4	1.48×10^6	3.77×10^4	1.48×10^6

Finally, the values of the dimensionless damping coefficient for the three orifice diameters, $D = 28, 31$ and 39 mm, calculated through Eq. (12), are $B^* = 160.49, 132.18$ and 84.85 , respectively.

3.3. Air compressibility effects

The values of the capture width ratio calculated for the 55 wave conditions tested under three damping conditions and two different set-ups, incompressible (assuming full geometric similarity) and compressible (scaling correctly the chamber air volume by enlarging it through an air reservoir), are presented in Figure 10. The effects of the air compressibility can be easily evaluated by comparing

the first and second column of graphs, or directly in the graphs of the third column which show the relative difference in the C_{WR} between the incompressible and compressible set-up.

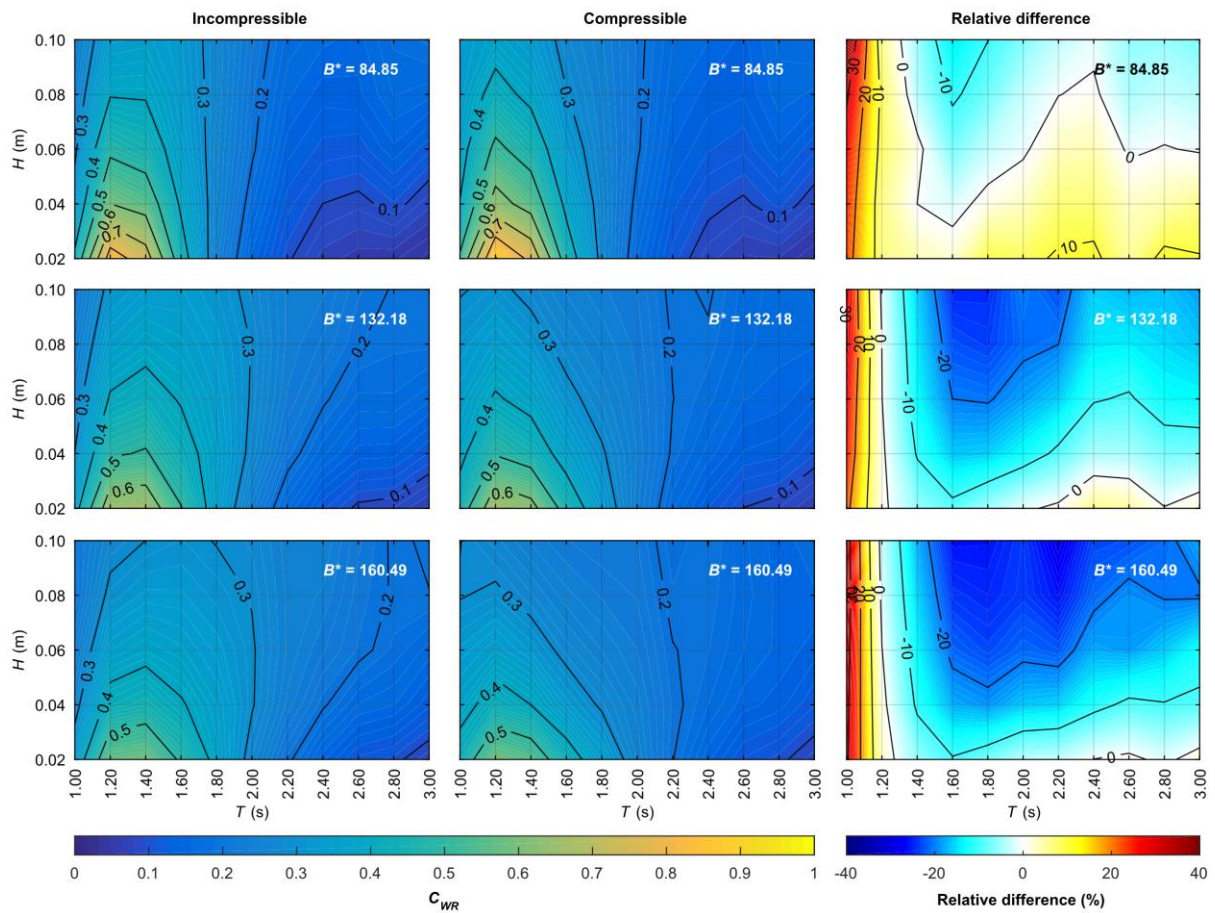


Figure 10. In the first and second column of graphs, variation of the capture width ratio (C_{WR}) with the wave height (H) and the wave period (T) under the three damping conditions tested, for the incompressible (first column) and compressible (second column) set-ups; in the third column, variation of the relative difference between the capture width ratio of the compressible set-up with respect to the incompressible one.

First, it could be interesting to analyse separately each set-up, incompressible and compressible. In the incompressible set-up (Figure 10 – left column), the results point that, for the OWC model tested, there is a resonant period (an optimum period which maximises the C_{WR}) in the vicinity of $T = 1.20\text{-}1.40$ s, that substantially improves the C_{WR} ; and the maximum performance is achieved for the lower wave heights. Second, the influence of the wave height is much more complex: for wave periods close to the resonant, the higher the wave height, the lower the C_{WR} ; on the contrary, for larger periods far away from the resonant (around $T = 3.0$ s), the higher the wave height, the greater the C_{WR} . For intermediate periods (around $T = 2.0$ s), the influence of the variation in wave height is much lower, producing only slight variations in the C_{WR} . Third, the damping, known to be a critical

parameter on the performance of an OWC (López, I. *et al.*, 2015), plays also an important role: an appropriate selection can improve the maximum capture width ratio from $C_{WR} < 60\%$ for the higher damping ($B^* = 160.49$) to $C_{WR} > 80\%$ for the lower damping ($B^* = 84.85$). There is not, though, a damping condition that is optimum for every wave condition, it varies depending on the wave height and period combination. All these findings are in accordance with those provided by previous works (e.g., López, I. *et al.*, 2015; Rezanejad *et al.*, 2017), contributing again to validate the methodology followed in this work.

Attending to the compressible set-up (Figure 10 – centre column), overall, all the previous results remain valid. This fact gives relevance to the incompressible testing, which constitutes a valid approach to obtain a general view of the performance of an OWC wave energy converter. However, a careful comparative analysis points out subtle differences. In this way, in the incompressible set-up, the resonant period changes depending both on the damping conditions and on the wave height. When the damping coefficient increases, the resonant period changes towards greater wave periods, e.g., for $B^* = 84.85$ and $H = 0.02$ m, the resonant period is $T = 1.20$ s, whereas for $B^* = 160.49$ and $H = 0.02$ m, the resonant period increases to $T = 1.40$ s. Moreover, it can be seen that the resonant period also moves to greater values when the wave height increases, e.g., for $H = 0.02$ m and $B^* = 132.18$ the resonant period is $T = 1.40$ s, whereas for $H = 0.10$ m and $B^* = 132.18$, the resonant period increases to $T = 1.60$ s. This behaviour becomes more evident for the greater values of the damping coefficient. In the compressible set-up, however, the resonant period remains constant at the same value ($T = 1.20$ s) independently of both the damping conditions and the wave height.

More importantly, the capture width ratio is also altered by the air compressibility effects, as indicates the relative difference between the C_{WR} of the compressible set-up with respect to the incompressible one (Figure 10 – right column). The results show that the influence of the air compressibility on the capture width ratio highly depends on the wave conditions. Thus, for the smaller wave periods ($T < 1.20$ s), the air compressibility exerts a positive influence on the C_{WR} , with improvements on the performance of the OWC higher than 30%. On the contrary, for greater periods ($T > 1.20$ s), the air compressibility produces a reduction of the C_{WR} up to -28.2% . In addition, the damping plays an important role, mainly for the wave conditions of $T > 1.20$ s: for the greater value of the damping coefficient ($B^* = 160.49$), air compressibility negatively impacts the C_{WR} for practically the whole range of wave heights; nevertheless, for the lower value of the damping coefficient ($B^* = 84.85$), the air compressibility effects are positive from the point of view of the C_{WR} for the

wave conditions with lower wave heights ($H < 0.06$ m). For these waves with greater period ($T > 1.20$ s), overall, the greater the wave height, the greater the negative impact of the air compressibility effects. This result is related to the findings of Simonetti *et al.*, (2018), who point that scaling effects due to air compressibility become more important as the pressure drop increases (in general, higher wave heights produce greater oscillations of the water column and, therefore, greater pressure differences).

Complementarily to the previous analysis, it is also interesting to establish the overall influence of air compressibility, by averaging the capture width ratio over the whole set of wave conditions for both set-ups, incompressible and compressible (Table 6). The relative difference between the global average values of the capture width ratio between the incompressible and compressible set-ups is about 10% for the greater values of the damping coefficient ($B^* = 132.18$ and 160.49), drastically changing for the lower damping condition ($B^* = 84.85$) under which the relative difference is positive and greater than 3%. Therefore, it is shown, again, that the damping plays an important role in the performance of an OWC converter, determining the direction of the overall influence of the air compressibility effects on the capture width ratio. Furthermore, when air compressibility effects are taken into account the optimum damping coefficient (i.e., that which maximises the C_{WR} for the whole set of wave conditions) changes: the optimum damping coefficient for the incompressible set-up is the intermediate one ($B^* = 132.18$), whereas for the compressible set-up is the lowest ($B^* = 84.85$). This is of paramount importance given that a wrong evaluation of the optimum damping could lead to a wrong dimensioning of the turbine (Pereiras *et al.*, 2015).

Table 6. Global average values of the capture width ratio (C_{WR}) considering the whole set of wave conditions, for the three values of the damping coefficient.

B^*	C_{WR}		<i>Relative difference (%)</i>
	<i>incompressible set-up</i>	<i>compressible set-up</i>	
160.49	0.278	0.250	−9.99
132.18	0.284	0.261	−8.08
84.85	0.256	0.265	+3.58

In the recent literature, only a couple of works focused on the effects of the air compressibility on the performance of an OWC considering non-linear effects (i.e., without analytical simplifications of the governing processes), both carried out by numerical modelling (Elhanafi *et al.*, 2017; Simonetti *et al.*, 2018). For the testing conditions (wave height, wave period and damping conditions) considered in these works, overestimations of the OWC performance in the order of 10% was found when air compressibility effects are disregarded. These works, however, only point to a negative

impact of the air compressibility, which is probably related to the reduced range of testing conditions considered. In any case, despite the limited conditions tested, Elhanafi *et al.* (2017) highlighted that the overestimation in OWC efficiency is more pronounced for wave periods larger than the resonant, and noted the influence of the damping conditions, results which are in line with those presented in this work. The complex nature of the air compressibility effects on the OWC performance was also pointed out, through an analytical model, by Falcão *et al.* (2014), who emphasise that disregarding air compressibility effects leads to errors which change its sign depending on the wave period.

4. Conclusions

In this work, the influence of air compressibility on the performance of an OWC wave energy converter was thoroughly evaluated through physical modelling. To take into account the air compressibility, the scaling of the air volume of the OWC chamber was performed according to the square of the length scale ratio ($V \propto \varepsilon^2$) using an air reservoir to provide the additional air volume required. Moreover, an incompressible set-up was also tested by assuming full geometric similarity ($V \propto \varepsilon^3$), i.e., disconnecting the air reservoir. The experimental campaign involved a total of 330 tests, resulting from the combination of 55 wave conditions and three different values of the turbine-induced damping, tested for two different set-ups, compressible and incompressible. The flow rate was calculated from pressure drop data measurements using calibrated pressure-vs-flow-rate curves for each of the three orifices which represent as many damping conditions. The calibration curves were obtained by means of the open source RANS-based CFD model OpenFOAM®, coupled with the *waves2Foam* toolbox for wave generation. The numerical model was successfully validated based on the experimental results (pressure drop and free surface elevation inside the OWC chamber), both quantitatively ($R_{average} > 0.98$, $NRMSE_{average} < 8\%$) and qualitatively (by direct comparison of the measurements from both models).

Based on the results of the experimental campaign, the following conclusions may be drawn. First, the incompressible set-up (i.e., full geometric similarity by scaling the air chamber volume to the cube of the length scale ratio) constitutes a useful approach to study an OWC in its early stages of development, for it leads to findings broadly similar to those obtained with the compressible set-up: (i) existence of a resonant period that maximises the capture width ratio (C_{WR}); (ii) significant influence of the damping on the C_{WR} ; and (iii) complex influence of the wave height on the C_{WR} , mainly governed by the wave period. However, disregarding air compressibility introduces spurious

variations of the resonant period when testing conditions change and, more importantly, leads to wrong estimates of the capture width ratio. Thus, although using an incompressible set-up could be a valid approach in the early stages of design, it must be avoided when an in-depth analysis of the performance of the OWC is required.

Second, the air compressibility effects significantly affect the efficiency of the OWC, altering the C_{WR} with respect to that of the incompressible set-up, approximately, in the range of -30 to 30 per cent, depending, mainly, on the wave conditions. Thus, air compressibility effects are highly influenced by the sea state. In general, disregarding air compressibility leads to underpredictions of the C_{WR} for periods below the resonant period, and to overpredictions for larger periods. Furthermore, it was shown that the damping plays a fundamental role in the performance of an OWC converter, determining the direction and magnitude of the overall influence of the air compressibility effects on the C_{WR} . It was also found that the optimum damping coefficient (critical parameter for dimensioning the turbine) decreases when air compressibility effects are taken into account; it follows that neglecting air compressibility could well lead to suboptimal specifications for the turbine. As a final remark, air compressibility effects are complex and, consequently, do not lend themselves to a simplification in the form of an overall percentage value – the variation of the performance of the OWC over the entire range of operating conditions must be considered.

In sum, the spring-like effect of air compressibility in the chamber is important in an OWC wave energy converter. Should this effect be disregarded, significant errors would be introduced in the assessment of the device efficiency, including both under- and over-predictions, depending on the sea state and the turbine-induced damping. In light of these results, it may be concluded that air compressibility must be considered in all but the preliminary stages of design or analysis.

Acknowledgements

During this work I. López was supported by the postdoctoral grant ED481B 2016/125-0 of the ‘Programa de Axudas á etapa posdoutoral da Xunta de Galicia (Consellería de Cultura, Educación e Ordenación Universitaria)’, and G. Iglesias benefited from a Marie Curie Individual Fellowship (WAVEIMPACT, PCIG13-GA-2013-618556). The authors are indebted to the Centre for Supercomputing of Galicia (CESGA), Spain, for the use of high-performance computational resources and the support in performing the numerical simulations.

Appendix A. Error estimators

The performance of the numerical model for each wave condition was evaluated on the basis of the correlation coefficient, defined as:

$$R = \frac{s_{xy}}{s_x s_y} \quad (\text{A.1})$$

where s_{xy} represents the covariance between the measurements from the experimental tests and the corresponding values from the numerical model tests; and s_x and s_y represent the sample standard deviation of the experimental and numerical tests, respectively. Additionally, the normalised root mean square error was also calculated as:

$$\text{NRMSE} = \frac{1}{x_{\max} - x_{\min}} \left[\frac{1}{N} \sum_{i=1}^N (x_i - y_i)^2 \right]^{1/2} \quad (\text{A.2})$$

where x_i represents the i -th data element of the measurements from the experimental tests; y_i represents the corresponding value from the numerical model tests; N is the total number of data points; and $x_{\max} - x_{\min}$ represent the range of the data from the experimental test considered. It is preferred over the average because of the sinusoidal nature of the data (the average is close to zero).

References

- Arena, F., Laface, V., Malara, G., Romolo, A., Viviano, A., Fiamma, V., et al., 2015. Wave climate analysis for the design of wave energy harvesters in the Mediterranean Sea. *Renew. Energy* 77, 125-141. <https://doi.org/10.1016/j.renene.2014.12.002>.
- Arena, F., Romolo, A., Malara, G., Ascanelli, A., 2013. On design and building of a U-OWC wave energy converter in the Mediterranean Sea: a case study. 32nd International Conference on Ocean, Offshore and Arctic Engineering (OMAE), Nantes, France, pp. V008T09A102. <https://doi.org/10.1115/OMAE2013-11593>.
- Astariz, S., Iglesias, G., 2015. The economics of wave energy: A review. *Renew. Sust. Energ. Rev.* 45, 397-408. <https://doi.org/10.1016/j.rser.2015.01.061>.
- Baquerizo, A., 1995. Wave reflection at beaches. PhD Thesis, University of Cantabria, Spain.
- Carballo, R., Sánchez, M., Ramos, V., Fraguera, J.A., Iglesias, G., 2015. Intra-annual wave resource characterization for energy exploitation: A new decision-aid tool. *Energy Conv. Manag.* 93, 1-8. <https://doi.org/10.1016/j.enconman.2014.12.068>.
- Contestabile, P., Di Lauro, E., Buccino, M., Vicinanza, D., 2017. Economic Assessment of Overtopping Breakwater for Energy Conversion (OBREC): A Case Study in Western Australia. *Sustainability* 9 (1), 51. <https://doi.org/10.3390/su9010051>.

639 Deshpande, S.S., Anumolu, L., Trujillo, M.F., 2012. Evaluating the performance of the two-phase
640 flow solver interFoam. *Comput.Sci.Disc.* 5 (1), 014016. [https://dx.doi.org/10.1088/1749-](https://dx.doi.org/10.1088/1749-4699/5/1/014016)
641 4699/5/1/014016.

642 Dixon, S.L., Hall, C.A., 2014. *Fluid Mechanics and Thermodynamics of Turbomachinery*.
643 Butterworth-Heinemann, Boston.

644 Elhanafi, A., Macfarlane, G., Fleming, A., Leong, Z., 2017. Scaling and air compressibility effects on
645 a three-dimensional offshore stationary OWC wave energy converter. *Appl.Energy* 189, 1-20.
646 <https://doi.org/10.1016/j.apenergy.2016.11.095>.

647 Falcão, A.F.O., Gato, L.M.C., 2012. 8.05 - Air Turbines. In: A. Sayigh (Ed.), *Comprehensive*
648 *Renewable Energy*, Elsevier, Oxford, pp. 111-149. [https://dx.doi.org/10.1016/B978-0-08-](https://dx.doi.org/10.1016/B978-0-08-087872-0.00805-2)
649 087872-0.00805-2.

650 Falcão, A.F.O., Henriques, J.C.C., 2014. Model-prototype similarity of oscillating-water-column
651 wave energy converters. *Int.J.Mar.Energy* 6, 18-34.
652 <https://dx.doi.org/10.1016/j.ijome.2014.05.002>.

653 Falcão, A.F.O., Henriques, J.C.C., 2016. Oscillating-water-column wave energy converters and air
654 turbines: A review. *Renew.Energy* 85, 1391-1424.
655 <https://dx.doi.org/10.1016/j.renene.2015.07.086>.

656 Falcão, A.F.O., Justino, P.A.P., 1999. OWC wave energy devices with air flow control. *Ocean Eng.*
657 26 (12), 1275-1295. [https://doi.org/10.1016/S0029-8018\(98\)00075-4](https://doi.org/10.1016/S0029-8018(98)00075-4).

658 Higuera, P., Lara, J.L., Losada, I.J., 2013. Simulating coastal engineering processes with
659 OpenFOAM®. *Coast.Eng.* 71, 119-134. <https://doi.org/10.1016/j.coastaleng.2012.06.002>.

660 Hirt, C.W., Nichols, B.D., 1981. Volume of fluid (VOF) method for the dynamics of free boundaries.
661 *J.Comput.Phys.* 39 (1), 201-225. [https://doi.org/10.1016/0021-9991\(81\)90145-5](https://doi.org/10.1016/0021-9991(81)90145-5).

662 Hu, Z.Z., Greaves, D., Raby, A., 2016. Numerical wave tank study of extreme waves and wave-
663 structure interaction using OpenFoam®. *Ocean Eng.*
664 126, 329-342. <https://doi.org/10.1016/j.oceaneng.2016.09.017>.

665 Hughes, S.A., 1993. *Physical models and laboratory techniques in coastal engineering*. World
666 Scientific, Singapore.

667 Ibarra-Berastegi, G., Sáenz, J., Ulazia, A., Serras, P., Esnaola, G., Garcia-Soto, C., 2018. Electricity
668 production, capacity factor, and plant efficiency index at the Mutriku wave farm (2014–2016).
669 *Ocean Eng.* 147, 20-29. <https://doi.org/10.1016/j.oceaneng.2017.10.018>.

670 Iglesias, G., Carballo, R., 2014. Wave farm impact: The role of farm-to-coast distance. *Renew.Energy*
671 69, 375-385. <https://dx.doi.org/10.1016/j.renene.2014.03.059>.

672 Iturrioz, A., Guanche, R., Lara, J.L., Vidal, C., Losada, I.J., 2015. Validation of OpenFOAM® for
673 Oscillating Water Column three-dimensional modeling. *Ocean Eng.*
674 107, 222-236. <https://doi.org/10.1016/j.oceaneng.2015.07.051>.

675 Jacobsen, N.G., Fuhrman, D.R., Fredsøe, J., 2012. A wave generation toolbox for the open- source
676 CFD library: OpenFoam®. *Int.J.Numer.Methods Fluids* 70 (9), 1073-1088.
677 <https://doi.org/10.1002/fld.2726>.

678 Jasak, H., Jemcov, A., Tukovic, Z., 2007. OpenFOAM: A C++ library for complex physics
679 simulations. International Workshop on Coupled Methods in Numerical Dynamics, Dubrovnik,
680 Croatia, pp. 1-20.

681 López, I., Pereiras, B., Castro, F., Iglesias, G., 2014. Optimisation of turbine-induced damping for an
682 OWC wave energy converter using a RANS–VOF numerical model. *Appl.Energy* 127, 105-114.
683 <https://doi.org/10.1016/j.apenergy.2014.04.020>.

684 López, I., Pereiras, B., Castro, F., Iglesias, G., 2015. Performance of OWC wave energy converters:
685 influence of turbine damping and tidal variability. *Int.J.Energy Res.* 39 (4), 472-483.
686 <https://doi.org/10.1002/er.3239>.

687 López, I., Pereiras, B., Castro, F., Iglesias, G., 2016. Holistic performance analysis and turbine-
688 induced damping for an OWC wave energy converter. *Renew.Energy* 85, 1155-1163.
689 <https://dx.doi.org/10.1016/j.renene.2015.07.075>.

690 López, M., Taveira-Pinto, F., Rosa-Santos, P., 2017. Numerical modelling of the CECO wave energy
691 converter. *Renew.Energy* 113, 202-210. <https://doi.org/10.1016/j.renene.2017.05.066>.

692 Mansard, E.P.D., Funke, E.R., 1980. The measurement of incident and reflected spectra using a least
693 squares method. 17th International Conference on Coastal Engineerig, Sydney, Australia, pp.
694 154-172. <https://doi.org/10.1061/9780872622647.008>.

695 Medina-López, E., Moñino, A., Borthwick, A.G.L., Clavero, M., 2017. Thermodynamics of an OWC
696 containing real gas. *Energy* 135, 709-717. <https://doi.org/10.1016/j.energy.2017.06.164>.

697 Moisel, C., Carolus, T.H., 2015. Novel mixed flow air-turbine for bidirectional operation in OWC
698 wave energy converters. 11th European Wave and Tidal Energy Conference (EWTEC), Nantes,
699 France, pp. 1-10.

700 Moisel, C., Carolus, T.H., 2014. Radial lift-based cascade for bi-directional wave energy air-turbines.
701 ASME Turbo Expo 2014: Turbine Technical Conference and Exposition, Düsseldorf, Germany,
702 pp. V02DT42A017. <https://dx.doi.org/10.1115/GT2014-25821>.

703 Ning, D., Wang, R., Zou, Q., Teng, B., 2016. An experimental investigation of hydrodynamics of a
704 fixed OWC Wave Energy Converter. *Appl.Energy* 168, 636-648.
705 <https://doi.org/10.1016/j.apenergy.2016.01.107>.

706 Pereiras, B., Castro, F., el Marjani, A., Rodriguez, M.A., 2011. An improved radial impulse turbine
707 for OWC. *Renew. Energy* 36 (5), 1477-1484. <https://doi.org/10.1016/j.renene.2010.10.013>.

708 Pereiras, B., López, I., Castro, F., Iglesias, G., 2015. Non-dimensional analysis for matching an
709 impulse turbine to an OWC (oscillating water column) with an optimum energy transfer. *Energy*
710 87, 481-489. <https://dx.doi.org/10.1016/j.energy.2015.05.018>.

711 Pérez-Collazo, C., Greaves, D., Iglesias, G., 2015. A review of combined wave and offshore wind
712 energy. *Renew.Sust.Energ.Rev.* 42, 141-153. <https://dx.doi.org/10.1016/j.rser.2014.09.032>.

713 Perez-Collazo, C., Greaves, D., Iglesias, G., 2018. A Novel Hybrid Wind-Wave Energy Converter for
714 Jacket-Frame Substructures. *Energies* 11 (3) <https://doi.org/10.3390/en11030637>.

715 Raghunathan, S., 1995. The wells air turbine for wave energy conversion. *Prog. Aerospace Sci.* 31
716 (4), 335-386. [https://doi.org/10.1016/0376-0421\(95\)00001-F](https://doi.org/10.1016/0376-0421(95)00001-F).

717 Reader-Harris, M., 2015. Orifice plates and venturi tubes. Springer International, Cham.

718 Rezanejad, K., Guedes Soares, C., López, I., Carballo, R., 2017. Experimental and numerical
719 investigation of the hydrodynamic performance of an oscillating water column wave energy
720 converter. *Renew.Energy* 106, 1-16. <https://doi.org/10.1016/j.renene.2017.01.003>.

721 Sarmiento, A., 1993. Model-test optimization of an OWC wave power plant. *Int.J.Offshore Polar Eng.*
722 3 (1), 66-72.

723 Sarmiento, A., Falcão, A.F.O., 1985. Wave generation by an oscillating surface-pressure and its
724 application in wave-energy extraction. *J.Fluid Mech.* 150, 467-485.
725 <https://doi.org/10.1017/S0022112085000234>.

726 Schäffer, H.A., Jakobsen, K.P., 2003. Non-linear wave generation and active absorption in wave
727 flumes. *Proc.Long Waves Symposium*, Thessaloniki, Greece, pp. 69-77.

728 Schmitt, P., Elsaesser, B., 2015. On the use of OpenFOAM to model oscillating wave surge
729 converters. *Ocean Eng.*
730 108, 98-104. <https://doi.org/10.1016/j.oceaneng.2015.07.055>.

731 Sheng, W., Alcorn, R., Lewis, A., 2013. On thermodynamics in the primary power conversion of
732 oscillating water column wave energy converters. *J.Renew.Sustain.Energy* 5 (2), 023105.
733 <https://doi.org/10.1063/1.4794750>.

734 Sheng, W., Lewis, A., 2018. Power takeoff optimization to maximize wave energy conversions for
735 Oscillating Water Column devices. *IEEE J.Ocean.Eng.* 43 (1), 36-47.
736 <https://doi.org/10.1109/JOE.2016.2644144>.

737 Sheng, W., Thiebaud, F., Babuchon, M., Brooks, J., Lewis, A., Alcorn, R., 2013. Investigation to air
738 compressibility of oscillating water column wave energy converters. 32nd International
739 Conference on Ocean, Offshore and Arctic Engineering, Nantes, France, pp. V008T9A005.
740 <https://doi.org/10.1115/OMAEE2013-10151>.

741 Sheng, W., Alcorn, R., Lewis, T., 2014. Physical modelling of wave energy converters. *Ocean Eng.*
742 84, 29-36. <https://doi.org/10.1016/j.oceaneng.2014.03.019>.

743 Simonetti, I., Cappietti, L., Elsafti, H., Oumeraci, H., 2017. Optimization of the geometry and the
744 turbine induced damping for fixed detached and asymmetric OWC devices: A numerical study.
745 *Energy* 139, 1197-1209. <https://doi.org/10.1016/j.energy.2017.08.033>.

746 Simonetti, I., Cappietti, L., Elsafti, H., Oumeraci, H., 2018. Evaluation of air compressibility effects
747 on the performance of fixed OWC wave energy converters using CFD modelling. *Renew.Energy*
748 119, 741-753. <https://doi.org/10.1016/j.renene.2017.12.027>.

749 Stansby, P., Carpintero Moreno, E., Stallard, T., Maggi, A., 2015. Three-float broad-band resonant
750 line absorber with surge for wave energy conversion. *Renew.Energy* 78, 132-140.
751 <https://doi.org/10.1016/j.renene.2014.12.057>.

752 Taveira-Pinto, F., Iglesias, G., Rosa-Santos, P., Deng, Z.D., 2015. Preface to special topic: Marine
753 Renewable Energy. *J.Renew.Sustain.Energy* 7 (6), 061601. <https://doi.org/10.1063/1.4939086>.

754 Thakker, A., Hourigan, F., Dhanasekaran, T.S., El, H.M., Usmani, Z., Ryan, J., 2004. Design and
755 performance analysis of impulse turbine for a wave energy power plant. *Int.J.Energy Res.* 29 (1),
756 13-36. <https://doi.org/doi.org/10.1002/er.1034>.

757 Vanneste, D., Troch, P., 2015. 2D numerical simulation of large-scale physical model tests of wave
758 interaction with a rubble-mound breakwater. *Coast.Eng.* 103, 22-41.
759 <https://doi.org/10.1016/j.coastaleng.2015.05.008>.

760 Viviano, A., Naty, S., Foti, E., Bruce, T., Allsop, W., Vicinanza, D., 2016. Large-scale experiments
761 on the behaviour of a generalised Oscillating Water Column under random waves.
762 *Renew.Energy*
763 99, 875-887. <https://doi.org/10.1016/j.renene.2016.07.067>.

764 Vyzikas, T., Deshoulières, S., Barton, M., Giroux, O., Greaves, D., Simmonds, D., 2017.
765 Experimental investigation of different geometries of fixed oscillating water column devices.
766 *Renew.Energy* 104, 248-258. <https://doi.org/10.1016/j.renene.2016.11.061>.

767 Vyzikas, T., Deshoulières, S., Giroux, O., Barton, M., Greaves, D., 2017. Numerical study of fixed
768 Oscillating Water Column with RANS-type two-phase CFD model. *Renew.Energy* 102, 294-
769 305. <https://doi.org/10.1016/j.renene.2016.10.044>.

770 Weber, J., 2007. Representation of non-linear aero-thermodynamic effects during small scale physical
771 modelling of OWC WECs. 7th European Wave and Tidal Energy Conference, Porto, Portugal,
772 pp. 11-14.

773

Table 1

Table 1. Dimensions of the geometrical parameters of the OWC model.

Geometrical parameter	Symbol	Model dimensions
Chamber height	h_c	63.6 cm
Chamber length (in the wave direction)	l_c	12.8 cm
Chamber width (transverse to wave direction)	w_c	65.0 cm
Entrance height	h_e	12.8 cm
Vertical walls thickness	t_z	2.0 cm
Horizontal walls thickness	t_x	2.8 cm
Orifice diameter	D	variable
Duct height	h_d	$25D$
Bedding height	h_b	8.0 cm
Bedding length	l_b	20.0 cm
Bedding slope	s	1:2

Table 2

Table 2. Wave conditions included in the numerical testing programme.

Wave condition	Model dimensions		Prototype dimensions	
	<i>T</i>	<i>H</i>	<i>T</i>	<i>H</i>
#1	1.20 s	0.06 m	6 s	1.5 m
#2	1.60 s	0.02 m	8 s	0.5 m
#3	1.60 s	0.04 m	8 s	1.0 m
#4	1.60 s	0.06 m	8 s	1.5 m
#5	1.60 s	0.08 m	8 s	2.0 m
#6	1.60 s	0.10 m	8 s	2.5 m
#7	2.00 s	0.06 m	10 s	1.5 m
#8	2.40 s	0.06 m	12 s	1.5 m
#9	2.80 s	0.06 m	14 s	1.5 m

Table 3

Table 3. Results of the numerical model validation based on the comparison between the experimental and numerical signals of pressure drop (Δp) and free surface elevation inside the OWC chamber (η_{OWC}).

<i>D</i> (mm)	Δp				η_{OWC}			
	<i>R</i>		NRMSE		<i>R</i>		NRMSE	
	<i>average</i>	<i>s</i>	<i>average</i>	<i>s</i>	<i>average</i>	<i>s</i>	<i>average</i>	<i>s</i>
28	0.9922	0.0044	0.0680	0.0186	0.9878	0.0044	0.0547	0.0131
31	0.9956	0.0073	0.0645	0.0204	0.9867	0.0050	0.0592	0.0117
39	0.9878	0.0097	0.0861	0.0316	0.9844	0.0113	0.0632	0.0159
	0.9919	0.0079	0.0729	0.0252	0.9863	0.0074	0.0590	0.0136

Table 4

Table 4. Results of the numerical model validation based on the comparison between the experimental and numerical signals of free surface elevation at two positions along the flume (η_{WG4} and η_{WG6}), for two different wave conditions.

<i>D</i> (mm)	<i>H</i> = 0.02 m, <i>T</i> = 1.6 s				<i>H</i> = 0.10 m, <i>T</i> = 1.6 s			
	η_{WG4}		η_{WG6}		η_{WG4}		η_{WG6}	
	<i>R</i>	NRMSE	<i>R</i>	NRMSE	<i>R</i>	NRMSE	<i>R</i>	NRMSE
28	0.9983	0.0635	0.9960	0.0379	0.9952	0.0816	0.9886	0.0806
31	0.9974	0.0665	0.9948	0.0443	0.9967	0.0859	0.9863	0.0835
39	0.9857	0.0718	0.9839	0.0708	0.9950	0.0823	0.9884	0.0776
	0.9938	0.0673	0.9916	0.0510	0.9956	0.0833	0.9878	0.0806

Table 5

Table 5. Inhalation, exhalation and representative values of the damping parameter (B) for the three orifice diameters tested.

D (mm)	B_{inh} (kg/m ⁷)		B_{exh} (kg/m ⁷)		B_r (kg/m ⁷)
	<i>average</i>	s	<i>average</i>	s	<i>average</i>
28	5.33×10^6	9.72×10^4	5.27×10^6	8.24×10^4	5.30×10^6
31	3.59×10^6	7.54×10^4	3.59×10^6	6.86×10^4	3.59×10^6
39	1.48×10^6	3.59×10^4	1.48×10^6	3.77×10^4	1.48×10^6

Table 6. Global average values of the capture width ratio (C_{WR}) considering the whole set of wave conditions, for the three values of the damping coefficient.

B^*	C_{WR}		<i>Relative difference (%)</i>
	<i>incompressible set-up</i>	<i>compressible set-up</i>	
160.49	0.278	0.250	−9.99
132.18	0.284	0.261	−8.08
84.85	0.256	0.265	+3.58

Figure 1

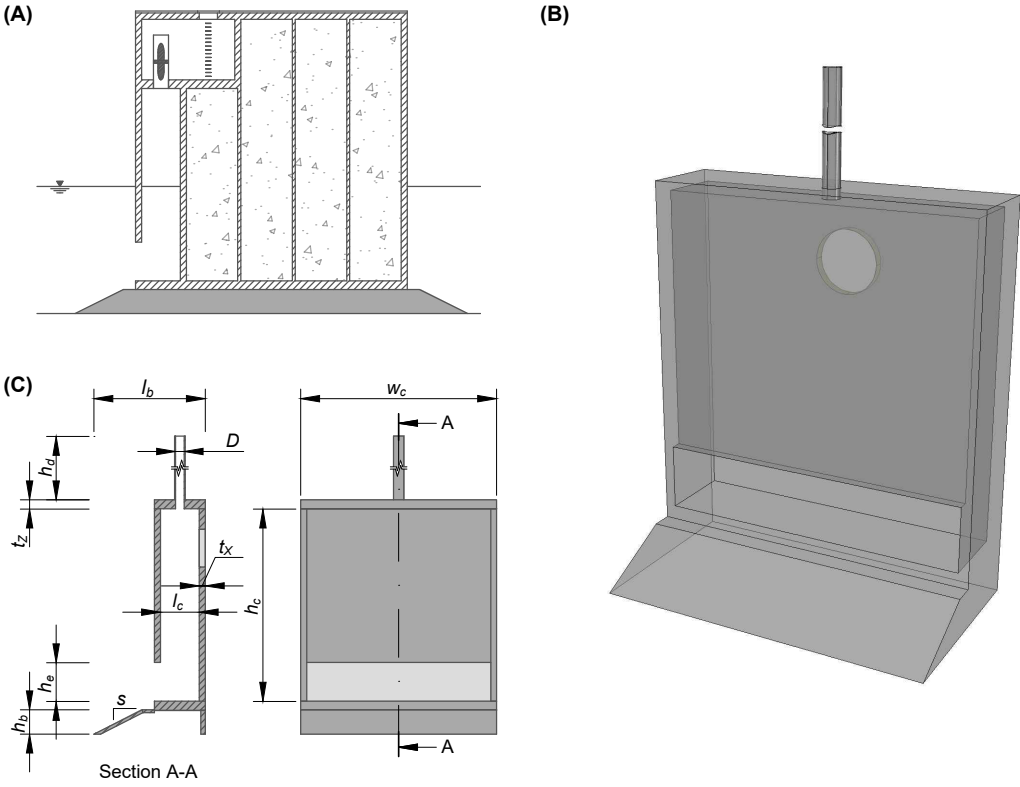


Figure 2

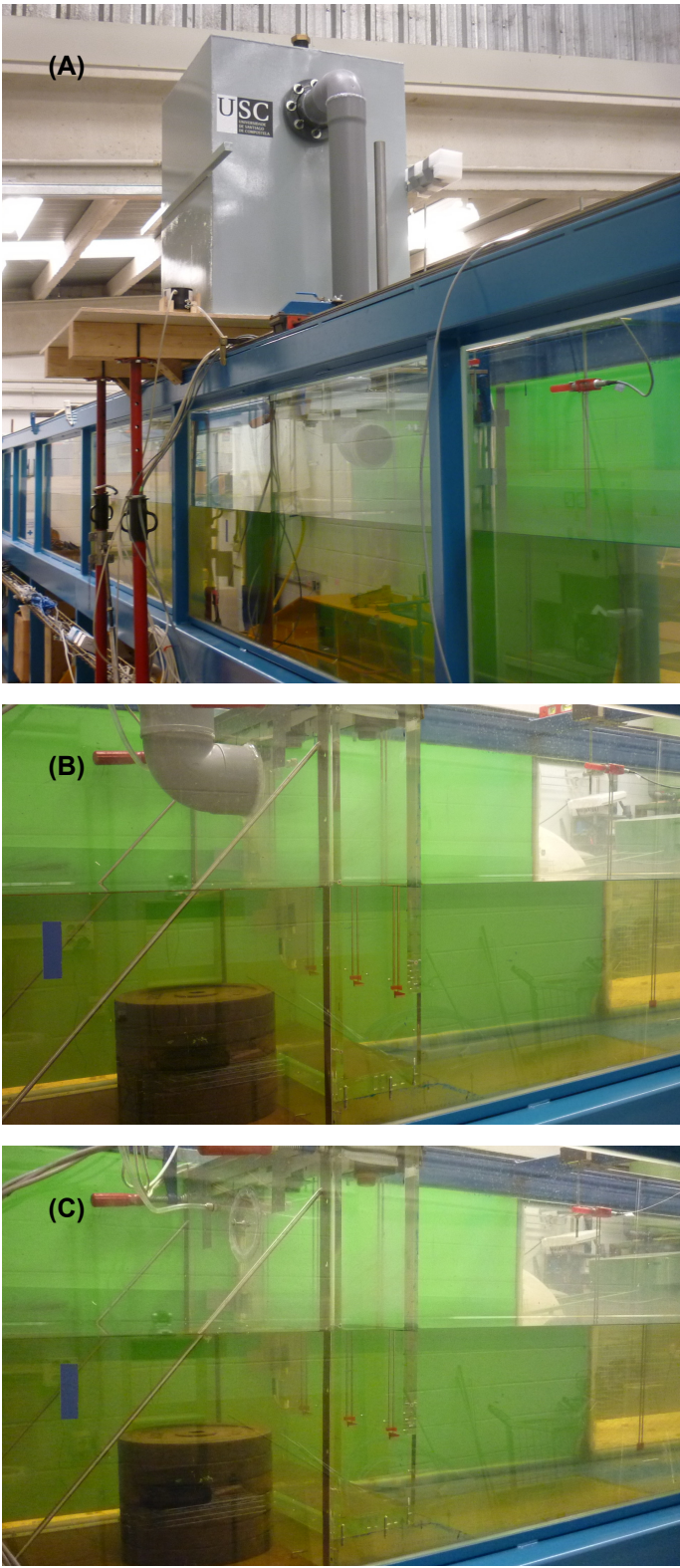


Figure 3

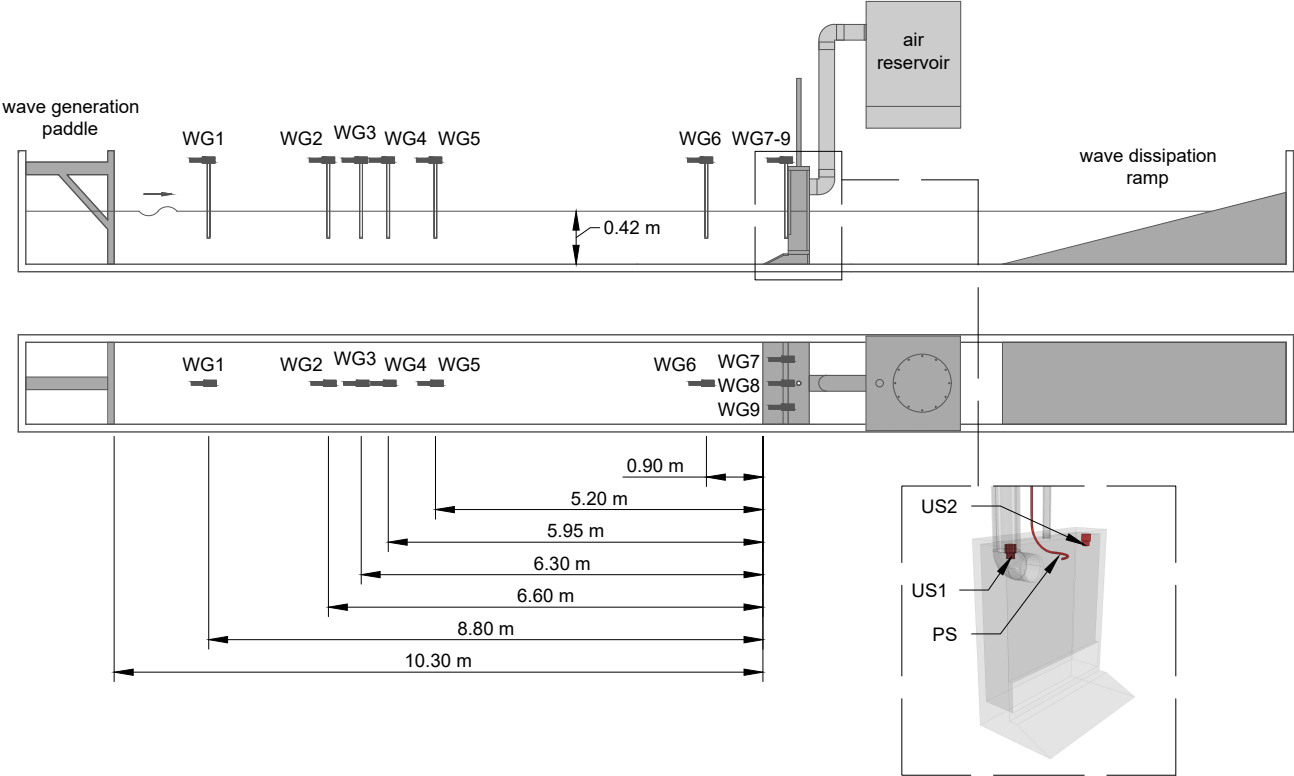


Figure 4

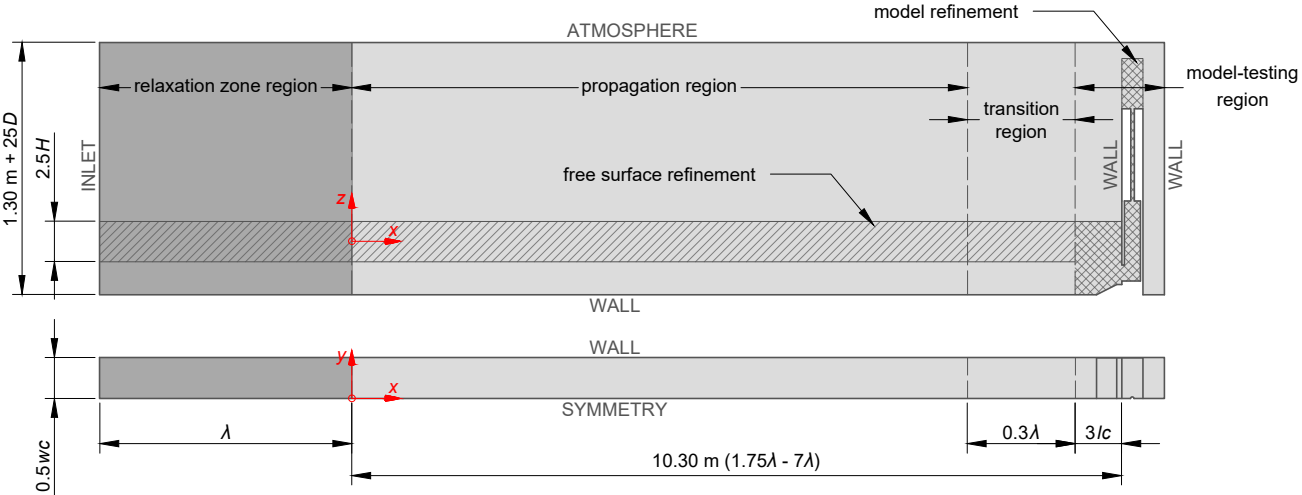


Figure 5

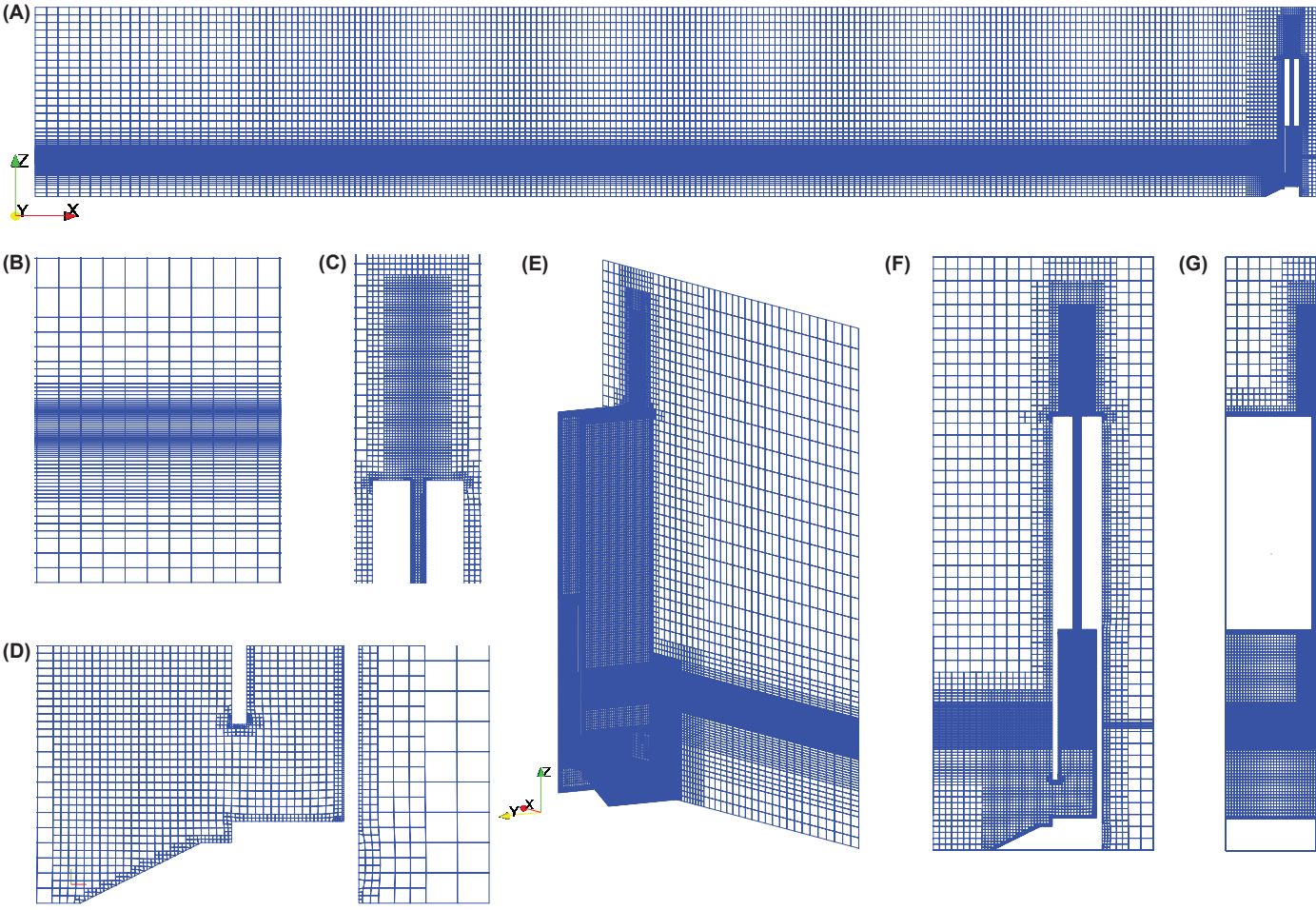


Figure 6

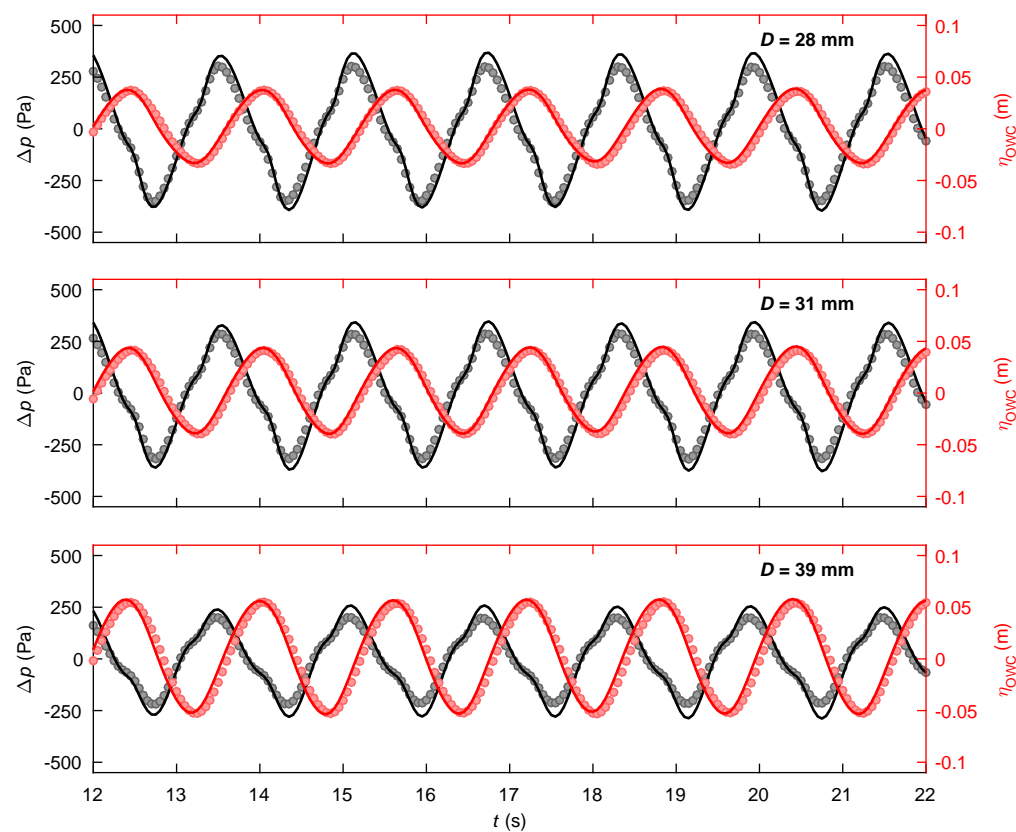


Figure 7

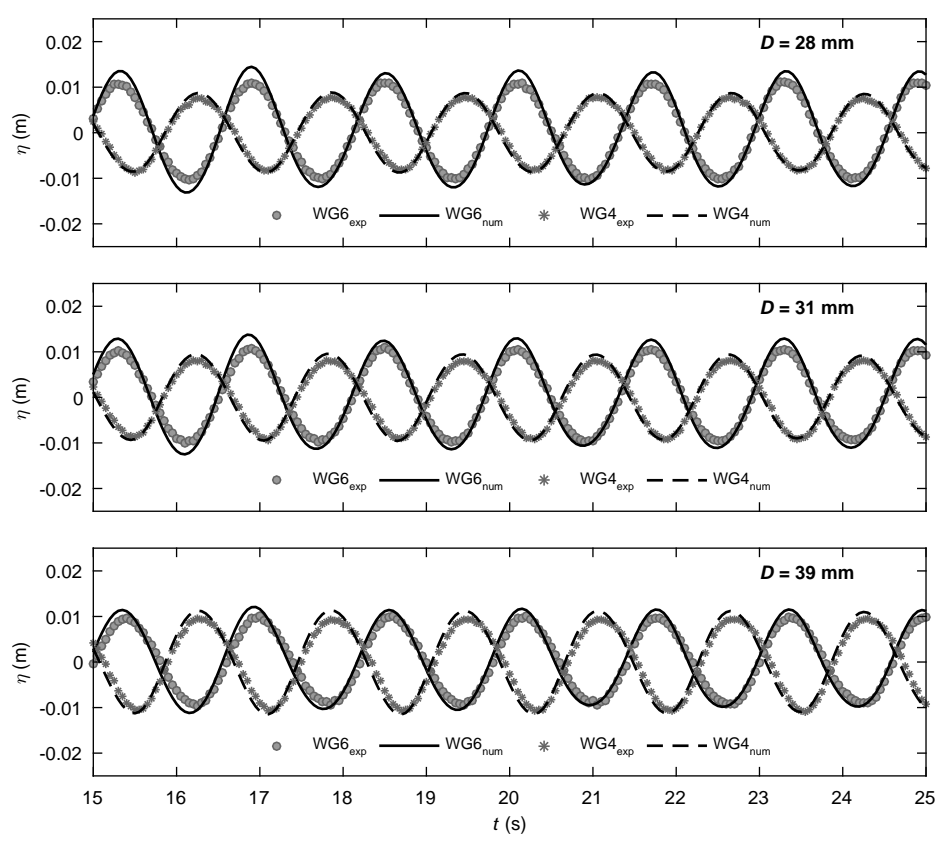


Figure 8

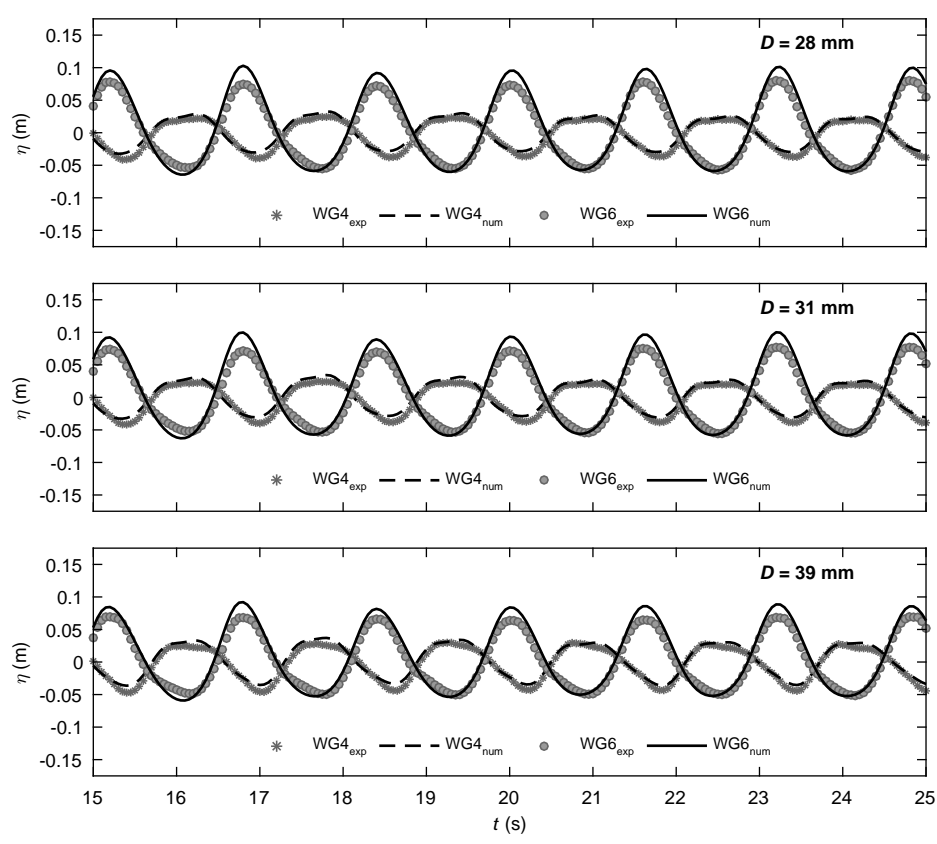


Figure 9

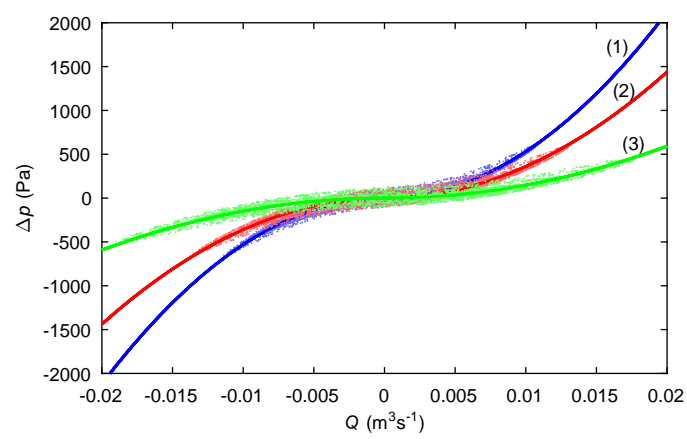


Figure 10

